earth

MDPI

Article

Trends of Climate Extremes and Their Relationships with Tropical Ocean Temperatures in South America

Luiz Octávio Fabrício dos Santos [1], Nadja Gomes Machado [2], Carlos Alexandre Santos Querino [3] and Marcelo Sacardi Biudes [4,*]

[1] Postgraduate Program in Environmental Physics, Institute of Physics, Federal University of Mato Grosso, 2367 Fernando Corrêa da Costa Ave., Cuiabá 78060-900, MT, Brazil; luizoctavio@fisica.ufmt.br
[2] Federal Institute of Mato Grosso, Juliano da Costa Marques Ave., Cuiabá 78050-560, MT, Brazil; nadja.machado@ifmt.edu.br
[3] Institute of Agriculture and Environment Education, Federal University of Amazonas, 786 29 de Agosto St., Humaitá 69800-000, AM, Brazil; carlosquerino@ufam.edu.br
[4] Institute of Physics, Federal University of Mato Grosso, 2367 Fernando Corrêa da Costa Ave., Cuiabá 78060-900, MT, Brazil
* Correspondence: marcelo@fisica.ufmt.br; Tel.: +55-65-99606-8893

Abstract: South America has experienced significant changes in climate patterns over recent decades, particularly in terms of precipitation and temperature extremes. This study analyzes trends in climate extremes from 1979 to 2020 across South America, focusing on their relationships with sea surface temperature (SST) anomalies in the Pacific and Atlantic Oceans. The analysis uses precipitation and temperature indices, such as the number of heavy rainfall days (R10mm, R20mm, R30mm), total annual precipitation (PRCPTOT), hottest day (TXx), and heatwave duration (WSDI), to assess changes over time. The results show a widespread decline in total annual precipitation across the continent, although some regions, particularly in the northeast and southeast, experienced an increase in the intensity and frequency of extreme precipitation events. Extreme temperatures have also risen consistently across South America, with an increase in both the frequency and duration of heat extremes, indicating an ongoing warming trend. The study also highlights the significant role of SST anomalies in both the Pacific and Atlantic Oceans in driving these climate extremes. Strong correlations were found between Pacific SST anomalies (Niño 3.4 region) and extreme precipitation events in the northern and southern regions of South America. Similarly, Atlantic SST anomalies, especially in the Northern Atlantic (TNA), exhibited notable impacts on temperature extremes, particularly heatwaves. These findings underscore the complex interactions between SST anomalies and climate variability in South America, providing crucial insights into the dynamics of climate extremes in the region. Understanding these relationships is essential for developing effective adaptation and mitigation strategies in response to the increasing frequency and intensity of climate extremes.

Keywords: climate extreme; atmospheric field analysis; climate change; trend analysis

Citation: dos Santos, L.O.F.; Machado, N.G.; Querino, C.A.S.; Biudes, M.S. Trends of Climate Extremes and Their Relationships with Tropical Ocean Temperatures in South America. *Earth* **2024**, *5*, 844–872. https://doi.org/10.3390/earth5040043

Academic Editor: Charles Jones

Received: 22 September 2024
Revised: 1 November 2024
Accepted: 7 November 2024
Published: 11 November 2024

1. Introduction

Earth's climate is undergoing significant changes, posing a major threat to populations worldwide. South America, with its vast geographic diversity and climate variability, is especially vulnerable to these changes [1]. The region contains a wide range of ecosystems, including tropical forests, savannas, deserts, and mountain ranges, all of which face distinct climate-related challenges [2]. As the frequency and intensity of extreme weather events increase, the societal, economic, and ecological impacts across South America are becoming more severe. Extreme events such as droughts, floods, storms, tropical cyclones, and heat waves are already causing significant damage to infrastructure, water resources, agriculture, and public health [3].

South America is one of the world's leading food-producing regions and is highly susceptible to climate extremes. These events directly threaten agricultural production, food security, and water resources, with cascading effects on energy, public supply, and economic activity [4]. Prolonged droughts exacerbate water scarcity, impacting agriculture and energy generation, while floods can contaminate drinking water and damage critical infrastructure [5]. Additionally, intense storms and tropical cyclones, with their destructive winds and heavy rainfall, lead to flash floods, posing significant risks to human life and property [6]. Heat waves further stress health systems, increase the risk of wildfires, and contribute to the spread of vector-borne diseases like dengue and malaria [1]. Understanding the connections between climate variability and extreme weather events is crucial for improving public health measures, managing water and energy resources, and enhancing community resilience. Therefore, studying extreme climate events in South America is essential for developing effective policies and actions to mitigate their impacts [7].

Addressing the complexity of climate change requires comprehensive and interdisciplinary mitigation and adaptation strategies. Collaboration among experts from various fields is critical, and decisions must be based on the best available scientific evidence [8]. However, the lack of tools to analyze long-term climate variables has limited our understanding of the global processes driving climate variability in South America [9]. Access to accurate climate data is essential for building a robust framework for climate resilience, which should include targeted adaptation strategies to reduce the region's vulnerability to diverse climate hazards.

Although several studies have examined climate extremes in different parts of South America [10–13], few have explored the potential effects of sea surface temperature (SST) anomalies or used unified datasets combining meteorological station data with interpolation techniques. Integrating observed data with climate models generates consistent time series for various climate variables, making these datasets, such as those from the Climate Prediction Center (CPC), valuable for long-term climate trend studies [14]. The CPC data, produced by one of the leading climate research centers in the United States, are widely used in forecasting and monitoring climate conditions globally. These data help inform decision-making in sectors such as agriculture, energy, and public safety [15].

Sea surface temperature (SST) oscillations, particularly in the Pacific and Atlantic Oceans, are key factors influencing extreme climate trends in South America [16]. The ocean plays a critical role in the global climate system, affecting atmospheric conditions and influencing temperature and precipitation patterns on continents. El Niño and La Niña events, driven by Pacific SST variations, cause significant shifts in atmospheric pressure and circulation, intensifying droughts and floods [17]. The Atlantic Ocean exhibits a recurring pattern of sea surface temperature (SST) anomalies, known as the Atlantic Dipole. In the Atlantic Ocean, the Atlantic Dipole, which alternates between positive and negative phases, impacts climate patterns by generating SST anomalies in the northern and southern hemispheres [18].

In this context, this study fills this gap by utilizing advanced climate data products, including those from the Climate Prediction Center (CPC), to analyze trends in precipitation and temperature extremes and their links to SST anomalies in both the Pacific and Atlantic Oceans.

2. Materials and Methods

2.1. Study Area: Climatological Features of IPCC Regions South America

This study utilizes the climate reference regions defined by the Sixth Assessment Report (AR6) of the Intergovernmental Panel on Climate Change (IPCC) for South America (SA) [19]. These regions represent distinct climate regimes and physiographic settings and are designed to maximize coverage by climate model grid boxes (Figure 1). Climate homogeneity is assessed based on temperature and precipitation gradients according to the Köppen–Geiger climate classification, as well as precipitation seasonality (Table 1).

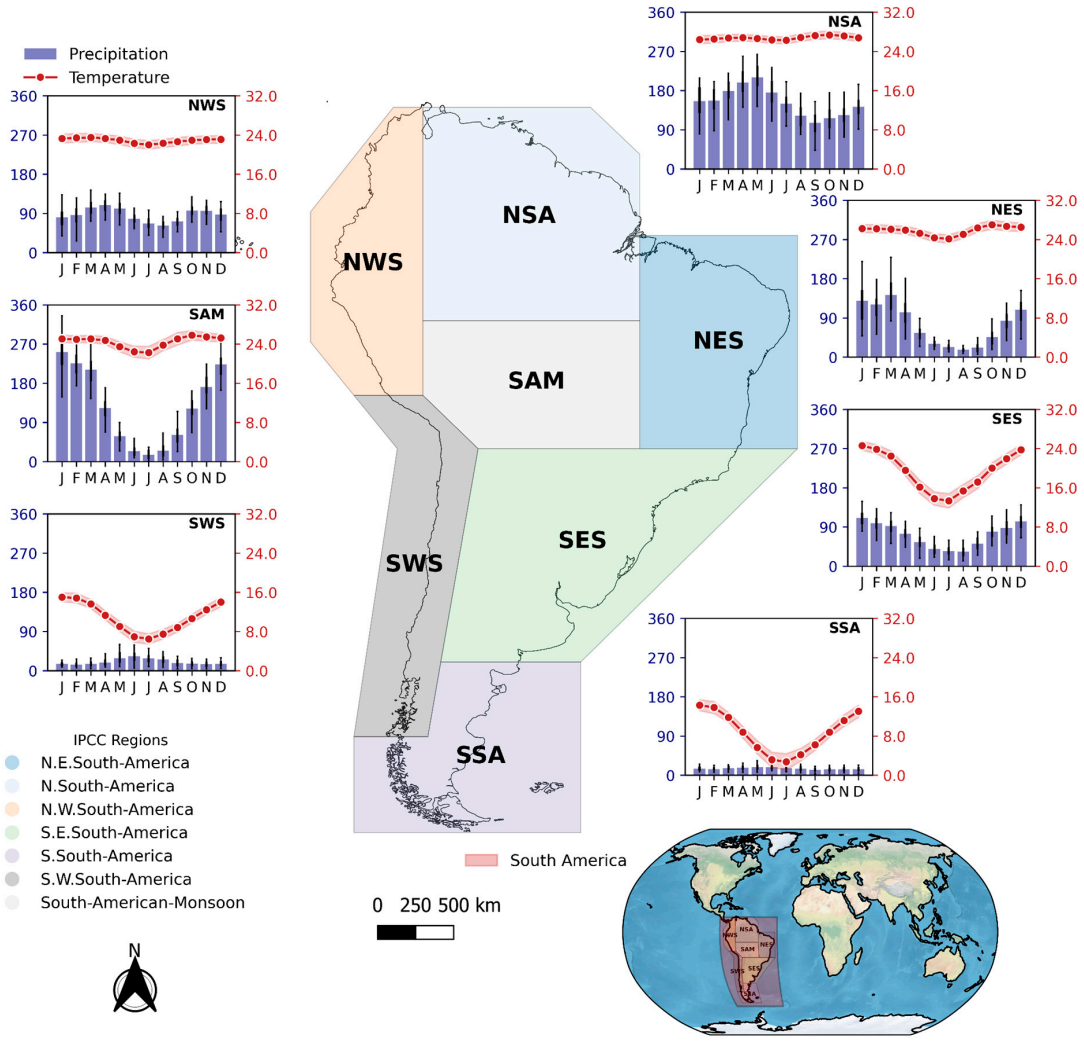

Figure 1. Climate normal for precipitation and air temperature and location of the climate reference regions from the Sixth Assessment Report of the Intergovernmental Panel on Climate Change (IPCC AR6) for South America from 1979 to 2020.

Table 1. Climatic Characteristics of South American Regions, based on the classification utilized by the Intergovernmental Panel on Climate Change (IPCC).

Region		Coverage Area	Precipitation Seasonality	Atmospheric Systems
NES	Northeast South America	Northeast Brazil	Highs in summer/autumn and lows in winter	Oceanic and atmospheric conditions—ENSO episodes in the Pacific Ocean and/or at an intense meridional sea surface temperature gradient over the tropical Atlantic—High-Level Cyclonic Vortex Episodes
NSA	Northern South America	Northern Brazilian Amazon, Eastern Colombia and Venezuela, Guyana, Suriname and French Guiana	Rainfall well distributed throughout the year (no drought). However, some locations do not have a clear rainy and dry season.	Seasonal meridional movement of the Pacific-Atlantic Intertropical Convergence Zone—Bolivian Upper
NWS	Northwest South America	Peru, Ecuador and Colombia		

Table 1. *Cont.*

Region		Coverage Area	Precipitation Seasonality	Atmospheric Systems
SES	Southeast South America	South, Southeast and part of the Brazilian Midwest, Paraguay, Uruguay and a large part of Argentina	Highs in summer and lows in winter	Transport of moisture from the Amazon by the action of the South American Low-Level Jet—Mesoscale convective systems—Surface cyclonic systems—Frontal systems—Instability lines—South Atlantic Convergence Zone
SSA	Southern South America	Extreme South of Argentina and Chile	Highs in winter and lows in summer	It depends on the position of the South Pacific Subtropical Anticyclone—an orographic barrier caused by the Andes.
SWS	Southwest South America	Southern Peru and almost all of Chile		
SAM	South American Monsoon	Southern Brazilian Amazon and part of the Midwest and Bolivia	A rainy season from October to March	Seasonal meridional movement of the Pacific and Atlantic Intertropical Convergence Zone—Bolivian Upper—South American Monsoon—South Atlantic Convergence Zone

2.2. Data

Daily precipitation, maximum and minimum air temperature, and monthly sea surface temperature (SST) data were obtained from January 1979 to December 2020. These datasets were sourced from the National Oceanic and Atmospheric Administration (NOAA) and made available by the Climate Prediction Center (CPC; https://psl.noaa.gov/data/gridded/, 10 accessed February 2021) (Table 2). The SST regions analyzed include Niño 1+2, Niño 3, Niño 3.4, Niño 4, Oceanic Niño Index (ONI), Tropical Northern Atlantic (TNA) and Tropical Southern Atlantic (TSA) (Figure 2).

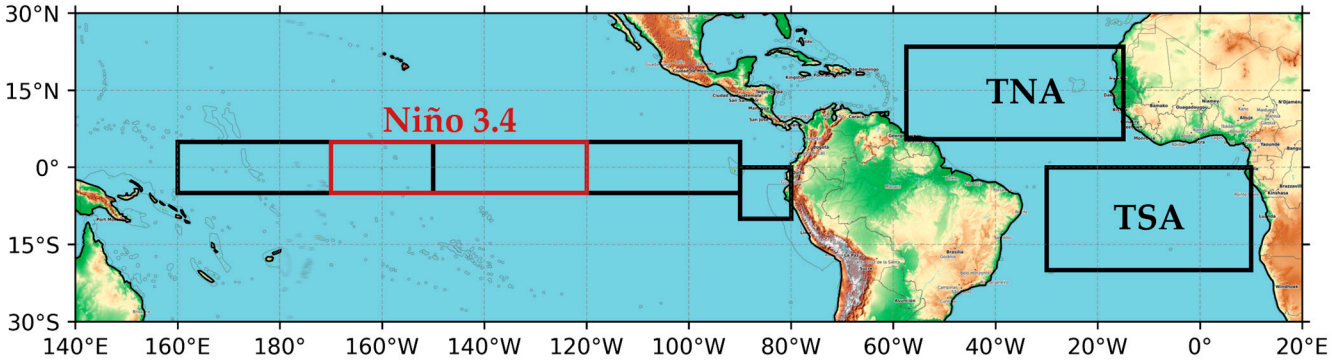

Figure 2. Location of the ENSO (Niño 1 + 2, Niño 3, Niño 3.4, and Niño 4) and Atlantic Dipole (TNA and TSA) regions in the equatorial Pacific and tropical Atlantic, respectively.

The CPC data products, particularly the Global Precipitation and Global Temperature datasets, provide consistent, high-quality data. These datasets are derived from ground-based stations, satellite observations, and advanced interpolation techniques [20,21]. The NOAA Extended Reconstruction Sea Surface Temperature (ERSST) version 5 dataset was used for SST data, which employs enhanced spatial and temporal reconstruction methods to ensure accuracy, especially in regions with sparse observations [22,23].

Table 2. Description of the precipitation, maximum and minimum temperature, and sea surface temperature datasets used for the study, from January 1979 to December 2020.

Variable	Dataset	Spatial Resolution	Period	Temporal Scale	Source/Reference
Precipitation	CPC—Global Precipitation	0.5 × 0.5	1 January 1979 to 31 December 2020	Daily	NOAA/Sun et al. [21]
Max-Min Temperature	CPC—Global Temperature	0.5 × 0.5	1 January 1979 to 31 December 2020	Daily	NOAA/CPC/Nashwan et al. [20]
Sea Surface Temperature	NOAA ERSST V5	2.5 × 2.5	1 January 1979 to 1 December 2020	Monthly	NOAA/Huang et al. [22]

2.3. Climate Extremes Indices

This study evaluates the interannual variability and long-term trends of extreme climate events using indices for precipitation and temperature extremes. The analysis focuses on the magnitude, severity, duration, and frequency of events such as heat waves, cold spells, and extreme rainfall. Precipitation extremes were assessed using indices such as the annual count of days with precipitation ≥10 mm, ≥20 mm, and ≥30 mm, along with the maximum one-day and five-day precipitation totals. Similarly, temperature extremes were analyzed based on maximum and minimum daily temperatures, as well as the duration and intensity of warm and cold periods [7].

We used the ClimPACT software to calculate the 27 extreme climate indices proposed by the Expert Team on Climate Change Detection Monitoring and Indices (ETCCDMI). ClimPACT software, developed by the Pacific Climate Impacts Consortium, to calculate 23 extreme climate indices, 11 derived from precipitation and 12 from temperature (Table 3). These indices are based on recommendations from the Expert Team on Climate Change Detection and Indices (ETCCDI) and are widely used for global climate assessments, allowing for international comparison [24].

Table 3. Description of extreme climate indices for precipitation and air temperature for the IPCC AR6 climate reference regions in South America. Tmax: maximum temperature; Tmin: minimum temperature; RR: daily precipitation; PRCP: total precipitation.

Variable	Index	ID	Definition	Units
Precipitation	Number of heavy precipitation days	R10mm	Annual count of days when PRCP ≥ 10 mm	days
	Number of very heavy precipitation days	R20mm	Annual count of days when PRCP ≥ 20 mm	days
	Number of days above nn mm	R30mm	Annual count of days when PRCP ≥ 30 mm	days
	Max 1-day precipitation amount	Rx1day	Annual max 1 day precipitation	mm
	Max 5-day precipitation amount	Rx5day	Annual max 5-day precipitation	mm
	Annual total wet day precipitation	PRCPTOT	Annual total PRCP in wet days—RR ≥ 1 mm	mm
	Simple daily intensity index	SDII	Annual total precipitation divided by the number of wet days—PRCP ≥ 1 mm	mm/day
	Precipitation on very wet days	R95p	Annual total precipitation (PRCP) when RR. 95th percentile	mm

Table 3. *Cont.*

Variable	Index	ID	Definition	Units
Precipitation	Precipitation on extremely wet days	R99p	Annual total PRCP when RR. 99th percentile	mm
	Consecutive wet days	CWD	Max number of consecutive days when RR $\geq$ 1 mm	days
	Consecutive dry days	CDD	Max number of consecutive days when RR < 1 mm	days
Air temperature	Warmest Day	TXx	Annual Maximum value of daily max temperature	°C
	Warmest Night	TNx	Annual Maximum value of daily min temperature	°C
	Coldest Day	TXn	Annual Minimum value of daily max temperature	°C
	Coldest Night	TNn	Annual Minimum value of daily min temperature	°C
	Diurnal Temperature Range	DTR	Daily Tmax—Daily Tmin	°C
	Warm spell duration	WSDI	Annual count of days with a least 6 consecutive days when Tmax > 90th percentile	days
	Cold spell duration	CSDI	Annual count of days with a least 6 consecutive days when Tmin < 10th percentile	days
	Warm Days	TX90p	% of days when Tmax is >90th percentile	%
	Warm Nights	TN90p	% of days when Tmin is >90th percentile	%
	Cool Days	TX10p	% of days when Tmax is <90th percentile	%
	Cool Nights	TN10p	% of days when Tmin is <90th percentile	%
	Frost Days	FD	Annual count of days when TN < 0 °C	days

2.4. Data Analysis

Trends in climate extremes were analyzed using the non-parametric Theil–Sen estimator [25], which is robust against non-normal data distributions [26]. The significance of these trends was tested using the modified Mann-Kendall (MMK) test, which accounts for autocorrelation in time series data, thus providing more reliable trend detection [27]. Correlations between SST anomalies and extreme climate indices were calculated using Pearson's correlation coefficient [28]. The significance of these correlations was adjusted for autocorrelation effects by estimating the effective degrees of freedom [29].

In addition, the probability density function (PDF) of the extreme climate indices was analyzed to assess shifts in the distributions of precipitation and temperature extremes over four decades: 1979–1988, 1989–1998, 1999–2008, and 2009–2020. The PDF method provides a non-parametric way to visualize changes in the frequency and intensity of extreme events across time, capturing shifts in both mean and variance [30].

3. Results

3.1. Trend of Extreme Indices

The IPCC-defined regions of South America (NSW, NSA, NES, SAM, SES, SWS, SSA) exhibit distinct patterns in precipitation and temperature extremes between 1979 and 2020 (Figures 3 and 4). In the northwest of South America (NSW), there has been a significant decrease in extreme precipitation events. The number of days with heavy precipitation (R10mm) declined by 2.80 days/year, and very heavy precipitation (R20mm) fell by 1.62 days/year. Precipitation on very wet (R95p) and extremely wet (R99p) days also

decreased by 37.51 mm/year and 11.91 mm/year, respectively (Figure 3). At the same time, the maximum temperature on the hottest day (TXx) showed a decreasing trend, while the coldest night (TNn) exhibited an increase, indicating a reduction in the diurnal temperature range (DTR) (Figure 4).

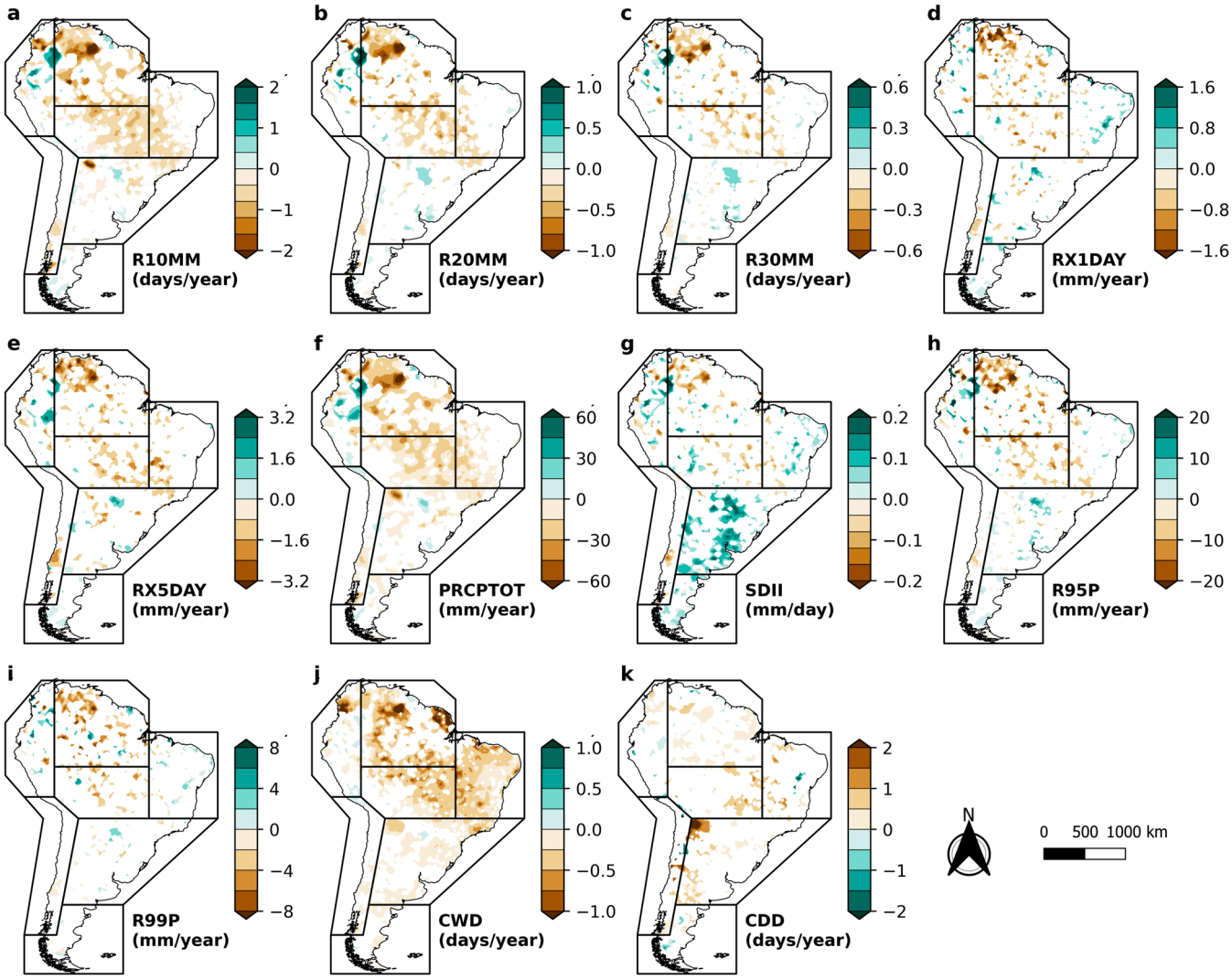

Figure 3. Spatial distribution of trends from 1979 to 2020: number of heavy precipitation days (R10mm) (**a**); number of very heavy precipitation days (R20mm) (**b**); number of days above 30 mm (R30mm) (**c**); max 1-day precipitation amount (Rx1day) (**d**); max 5-day precipitation amount (Rx5day) (**e**); annual total wet day precipitation (PRCPTOT) (**f**); simple daily intensity index (SDII) (**g**); precipitation on very wet days (R95p) (**h**); precipitation on extremely wet days (R99p) (**i**); consecutive wet days (CWD) (**j**); and consecutive dry days (CDD) (**k**) over the climate reference regions of the Sixth Assessment Report of the Intergovernmental Panel on Climate Change (IPCC—AR6) on South America. Only values with statistical significance at the 5% level are presented in the maps.

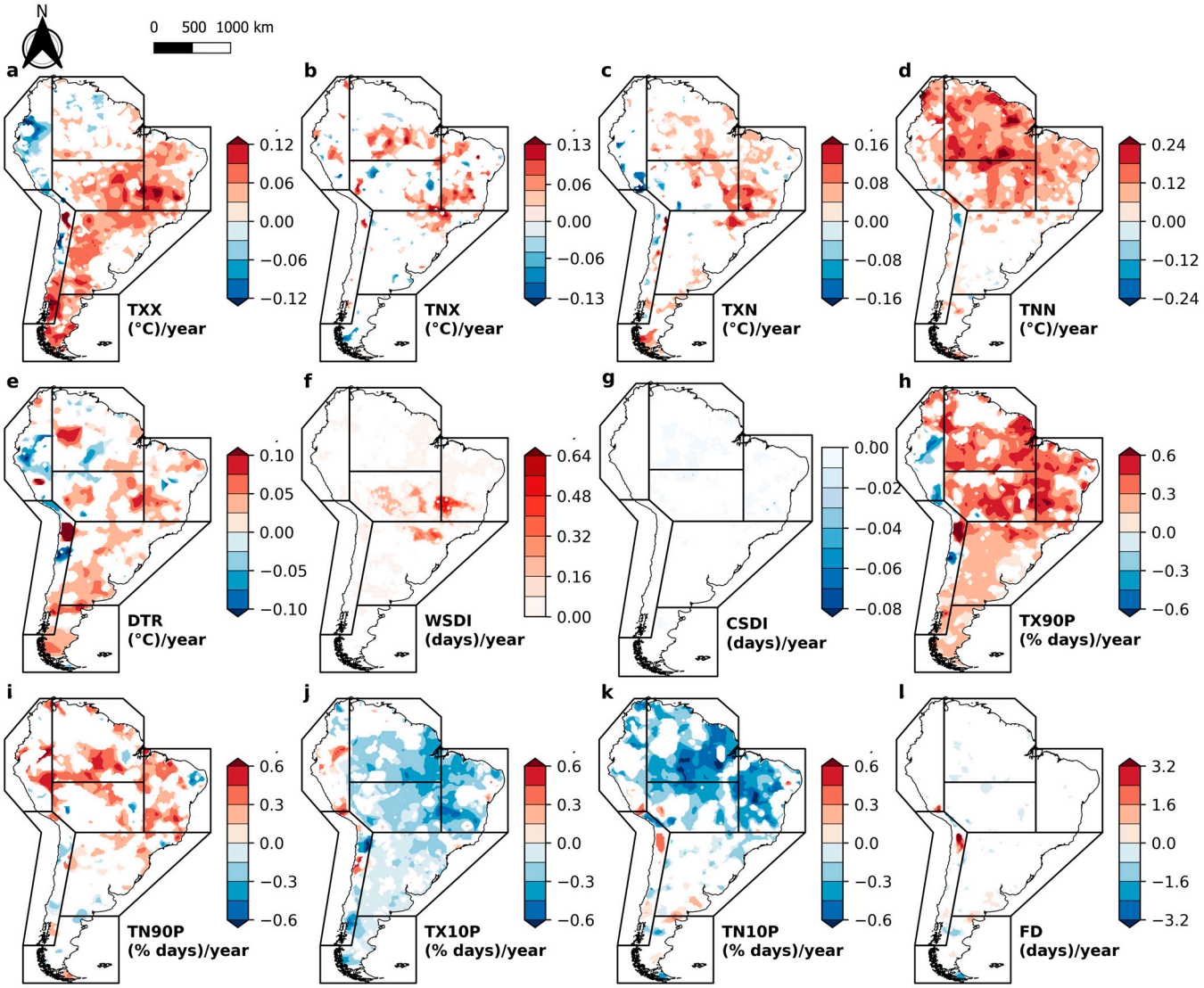

Figure 4. Spatial distribution of trends from 1979 to 2020: warmest day (TXx) (**a**); warmest night (TNx) (**b**); coldest day (TXn) (**c**); coldest night (TNn) (**d**); diurnal temperature Range (DTR) (**e**); warm spell duration (WSDI) (**f**); cold spell duration (CSDI) (**g**); warm days (TX90p) (**h**); warm nights (TN90p) (**i**); cool days (TX10p) (**j**); cool nights (TN10p) (**k**); and frost days (FD) (**l**) over the climate reference regions of the Sixth Assessment Report of the Intergovernmental Panel on Climate Change (IPCC—AR6) on South America. Only values with statistical significance at the 5% level are presented in the maps.

In northern South America (NSA), extreme precipitation indices also showed a marked decrease. The frequency of intense precipitation (R10mm and R20mm) dropped by 3.03 and 2.00 days/year, respectively, along with a significant reduction of 89 mm/year in total annual precipitation (PRCPTOT). However, the intensity of daily rainfall, as measured by the simple daily intensity index (SDII), showed a slight increase (Figure 3). In terms of temperatures, this region experienced an increase in both warm days (TX90p) and warm nights (TN90p), with corresponding decreases in cold days (TX10p) and cold nights (TN10p), indicating a general warming trend (Figure 4).

In northeast South America (NES), while some extreme precipitation indices showed negative trends, such as a reduction of 1.29 days/year for R10mm, the maximum one-day precipitation (RX1day) increased by 1.51 mm/year. The region also experienced a significant reduction in consecutive wet days (CWD), contributing to longer dry spells

(Figure 3). Regarding temperature, NES showed a marked increase in both warm days and warm nights, leading to more frequent and intense heat waves (WSDI). Cold events (TX10p, TN10p) became less frequent, suggesting that lower temperatures are becoming increasingly rare in this region (Figure 4).

The South American monsoon (SAM) region presented mixed results for precipitation extremes, with both positive and negative trends in daily rainfall intensity (SDII). However, there were clear reductions in total annual precipitation (PRCPTOT) and consecutive wet days (CWD), indicating an overall increase in dry extremes (Figure 3). Temperature extremes in SAM, on the other hand, showed consistent warming trends, with increased maximum and minimum temperatures, more frequent warm days and nights (TX90p, TN90p), and extended heat waves (WSDI) (Figure 4).

In southeastern South America (SES), the trends in extreme precipitation were characterized by high spatial variability. While some areas saw an increase in daily rainfall intensity (SDII), others experienced more frequent extreme precipitation events (R10mm, R20mm, R30mm) (Figure 3). Temperature trends pointed to a general increase in the frequency of heat waves and warm days, with TX90p and WSDI showing consistent upward trends. At the same time, the number of cold days (TX10p) showed a marked decrease (Figure 4).

In southwestern South America (SWS), the trends in precipitation extremes were relatively stable, with only slight increases in intense precipitation (R20mm) and daily rainfall intensity (SDII). However, the region saw the largest increase in consecutive dry days (CDD) across South America, averaging an additional 9.19 days/year (Figure 3). Temperature extremes showed a notable increase in both warm and cold extremes, with TX90p and frost days (FD) increasing significantly, indicating that SWS is sensitive to both hot and cold temperature extremes (Figure 4).

In southern South America (SSA), most precipitation indices exhibited negative trends, except for SDII, which showed a modest increase in daily rainfall intensity (Figure 3). This region experienced warming trends in maximum and minimum temperatures, with TXx and TX90p increasing. Frost days (FD) also showed a decreasing trend, suggesting that SSA is becoming more prone to heat extremes while experiencing fewer cold events (Figure 4).

3.2. Probability Density of Extreme Indices

The probability density function (PDF) analysis revealed significant changes in the distribution of extreme precipitation events over time. The number of heavy precipitation days (R10mm, R20mm, R30mm) showed a leftward shift, indicating fewer days with intense rainfall in recent decades. For instance, R10mm averaged 40 days/year in the most recent decade (2009–2020), compared to previous decades (Figure 5). Similar trends were observed for maximum one-day (Rx1day) and five-day precipitation totals (Rx5day), which also showed a consistent reduction across time (Figure 5).

For temperature extremes, the PDFs of warmest day (TXx), coldest day (TXn), and coldest night (TNn) shifted rightward, indicating an overall increase in temperature extremes. The diurnal temperature range (DTR) also increased each decade, with a mean rise of 0.41 °C between 1979 and 2020 (Figure 6). The warm spell duration index (WSDI) exhibited high variability, particularly in the SAM and NES regions, suggesting an increase in the duration of heat waves in these areas (Figure 6).

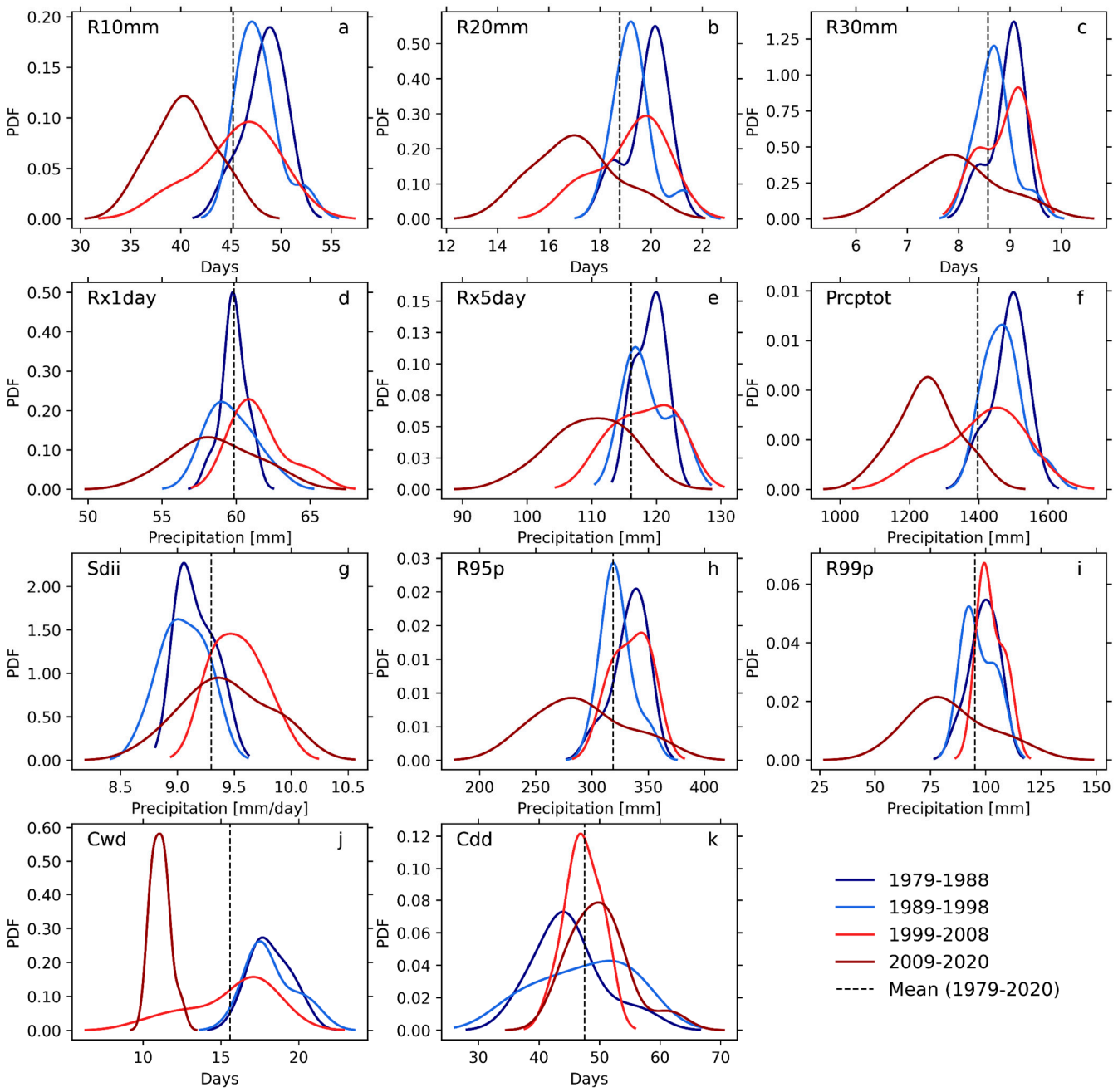

Figure 5. Probability density function (PDF) of the annual frequency of the following extreme precipitation indices over South America from 1979 to 2020: number of heavy precipitation days (R10mm) (**a**); number of very heavy precipitation days (R20mm) (**b**); number of days with precipitation above 50 mm (R50mm) (**c**); maximum 1-day precipitation amount (Rx1day) (**d**); maximum 5-day precipitation amount (Rx5day) (**e**); annual total wet-day precipitation (PRCPTOT) (**f**); simple daily intensity index (SDII) (**g**); precipitation on very wet days (R95p) (**h**); precipitation on extremely wet days (R99p) (**i**); consecutive wet days (CWD) (**j**); consecutive dry days (CDD) (**k**).

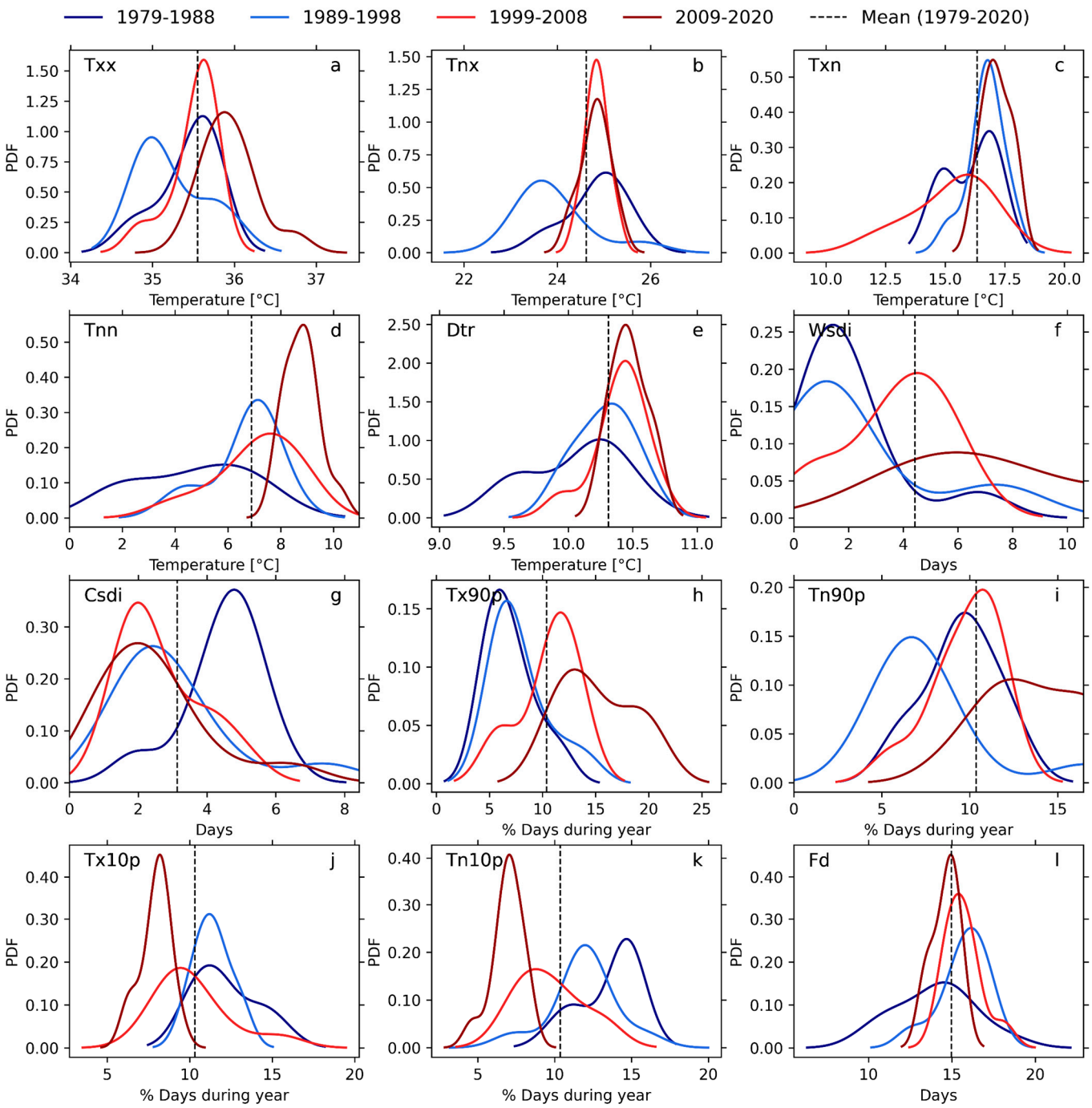

Figure 6. Probability density function (PDF) of the annual frequency of the following extreme temperature indices over South America from 1979 to 2020: warmest day (TXx) (**a**); warmest night (TNx) (**b**); coldest day (TXn) (**c**); coldest night (TNn) (**d**); diurnal temperature range (DTR) (**e**); warm spell duration (WSDI) (**f**); cold spell duration (CSDI) (**g**); warm days (TX90p) (**h**); warm nights (TN90p) (**i**); cool days (TX10p) (**j**); cool nights (TN10p) (**k**) and frost days (FD) (**l**).

3.3. Extremes Indices and Sea Surface Temperature (SST)

Extreme precipitation events across South America (SA) showed significant correlations with sea surface temperature (SST) anomalies, with correlation coefficients ranging from weak (0.3 to 0.49), to moderate (0.5 to 0.69), to strong (0.7 to 0.89). The spatial pattern of these correlations with the Niño 3.4 region was clearly defined (Figure 7), particularly in the northern (NSA), northeastern (NES), and southeastern (SES) regions of the conti-

nent, where strong correlations were observed between Pacific SST anomalies and extreme precipitation events.

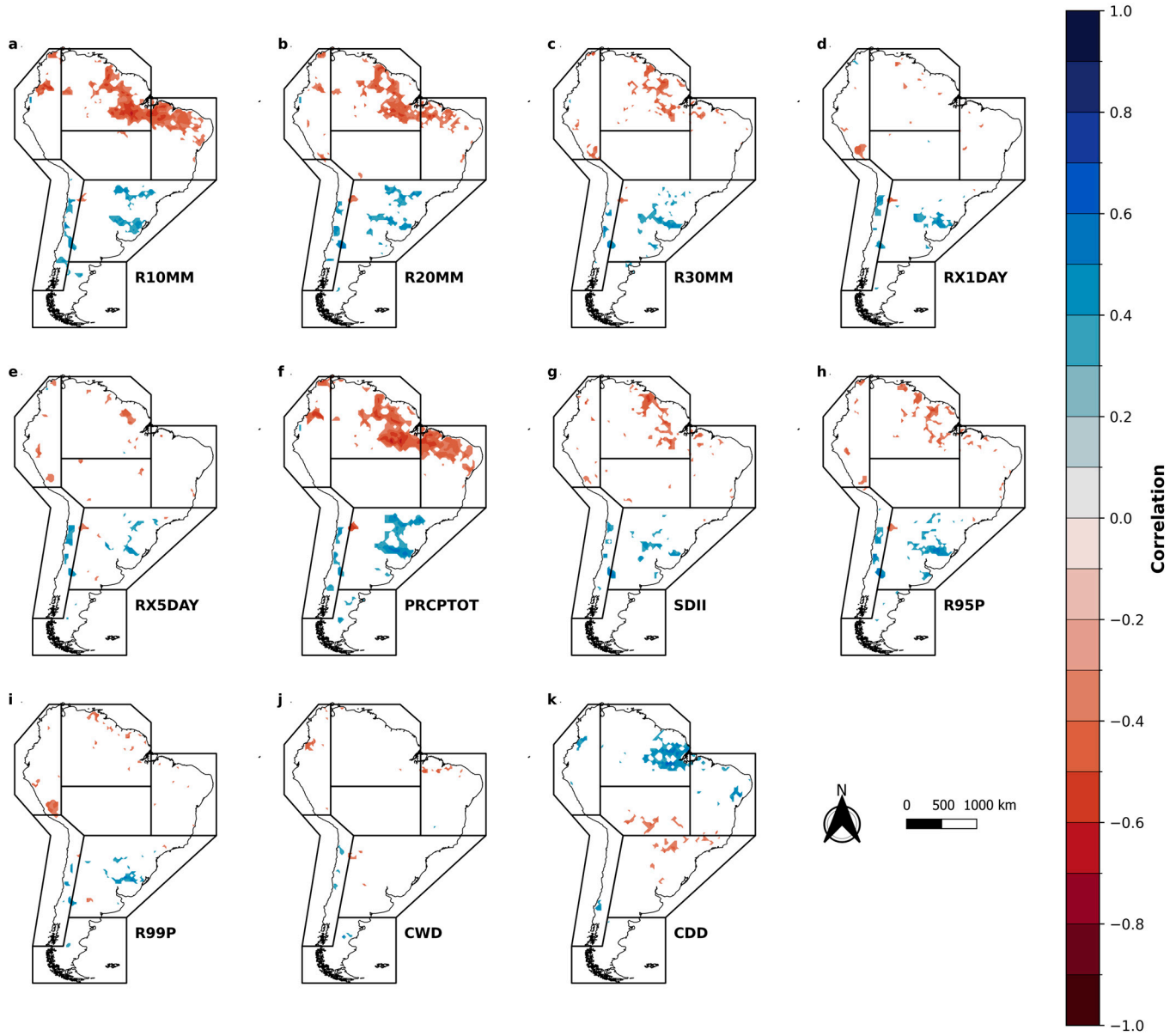

Figure 7. Pearson correlations between Pacific SST anomalies in the Niño 3.4 region and extreme precipitation indices: number of heavy precipitation days (R10mm) (**a**); number of very heavy precipitation days (R20mm) (**b**); number of days above 30 mm (R30mm) (**c**); max 1-day precipitation amount (Rx1day) (**d**); max 5-day precipitation amount (Rx5day) (**e**); annual total wet day precipitation (PRCPTOT) (**f**); simple daily intensity index (SDII) (**g**); precipitation on very wet days (R95p) (**h**); precipitation on extremely wet days (R99p) (**i**); consecutive wet days (CWD) (**j**); and consecutive dry days (CDD) (**k**) over the climate reference regions of the Sixth Assessment Report of the Intergovernmental Panel on Climate Change (IPCC—AR6) on South America from 1979 to 2020. Only values with statistical significance at the 5% level are presented in the maps.

Extreme precipitation events, such as intense rainfall days (R10mm, R20mm, R30mm) and total annual precipitation on wet days (PRCPTOT), showed strong correlations with Pacific SST anomalies. Notably, precipitation extremes were more pronounced during La Niña events, especially when combined with the negative phase of the Atlantic Dipole (Figures 7 and 9). There were also some relationships with neutral climate phases, though

these were less consistent. In the Atlantic Ocean, correlations between SST anomalies and precipitation extremes exhibited notable spatial variability. Indices such as intense rainfall (R10mm), daily precipitation intensity (SDII), total annual precipitation (PRCPTOT), and consecutive dry (CDD) and wet (CWD) days varied in intensity across regions. The SDII index showed an inverse pattern, with moderate positive correlations across much of South America, reflecting the complex dynamics between rainfall extremes and SST fluctuations in the Atlantic Ocean (Figure 8).

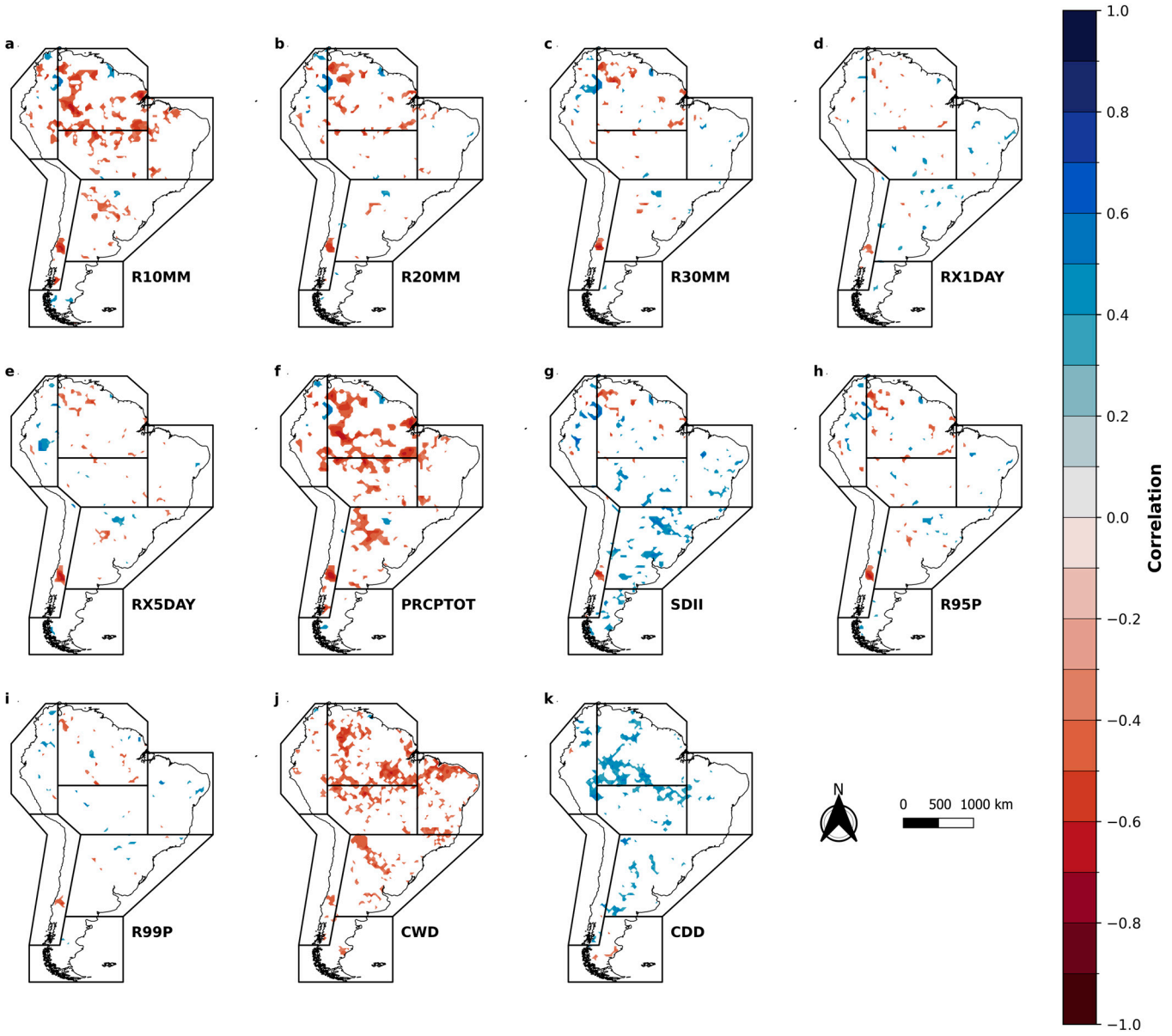

Figure 8. Pearson correlations between Atlantic SST anomalies in the Northern Atlantic Ocean (TNA) sector and extreme precipitation indices: number of heavy precipitation days (R10mm) (**a**); number of very heavy precipitation days (R20mm) (**b**); number of days above 30 mm (R30mm) (**c**); max 1-day precipitation amount (Rx1day) (**d**); max 5-day precipitation amount (Rx5day) (**e**); annual total wet day precipitation (PRCPTOT) (**f**); simple daily intensity index (SDII) (**g**); precipitation on very wet days (R95p) (**h**); precipitation on extremely wet days (R99p) (**i**); consecutive wet days (CWD) (**j**); and consecutive dry days (CDD) (**k**) over the climate reference regions of the Sixth Assessment Report of the Intergovernmental Panel on Climate Change (IPCC—AR6) on South America from 1979 to 2020. Only values with statistical significance at the 5% level are presented in the maps.

In general, extreme precipitation indices reached their highest and lowest values during simultaneous ENSO and Atlantic Dipole events, although some also occurred during neutral SST phases. Specifically, indices such as R10mm, R20mm, R30mm, RX5day, R95p, CWD, and PRCPTOT exhibited their maximum values during La Niña events combined with the negative phase of the Atlantic Dipole. On the other hand, SDII increased during La Niña events associated with the positive phase of the Atlantic Dipole (Figure 9).

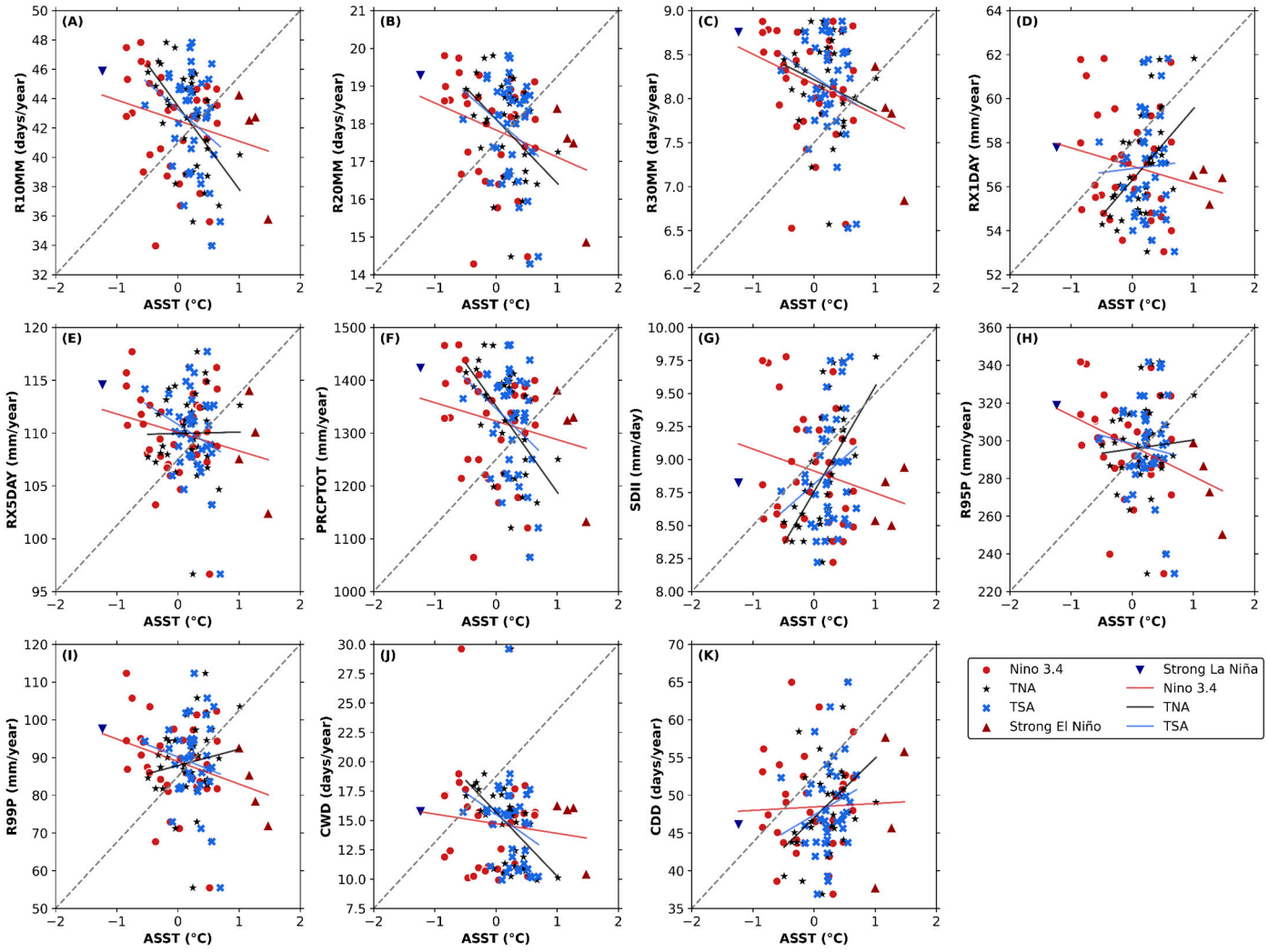

Figure 9. Relationship between sea surface temperature (SST) anomalies in the Pacific Ocean (Niño 3.4), Northern and Southern Atlantic Ocean sectors (TNA) (TSA), and extreme climate precipitation indices: number of heavy precipitation days (R10mm) (**A**); number of very heavy precipitation days (R20mm) (**B**); number of days above 30 mm (R30mm) (**C**); max 1-day precipitation amount (Rx1day) (**D**); max 5-day precipitation amount (Rx5day) (**E**); annual total wet day precipitation (PRCPTOT) (**F**); simple daily intensity index (SDII) (**G**); precipitation on very wet days (R95p) (**H**); precipitation on extremely wet days (R99p) (**I**); consecutive wet days (CWD) (**J**); and consecutive dry days (CDD) (**K**) over South America from 1979 to 2020.

In contrast, extreme precipitation indices tended to decrease during neutral SST periods and El Niño events, regardless of the Atlantic Dipole phase. This suggests a potential inhibition of extreme precipitation under these conditions. Minimum values for R10mm, R20mm, R30mm, and PRCPTOT were observed during years of Pacific SST neutrality combined with the negative phase of the Atlantic Dipole. Additionally, SDII decreased during periods of Pacific SST neutrality and a positive Atlantic Dipole. Frequency and intensity indices, such as R95p and R99p, also recorded reduced values during El Niño events associated with a positive Atlantic Dipole phase (Figure 9).

It is important to note that regional responses to El Niño, La Niña, and Atlantic Dipole events vary, with different degrees of association. Generally, extreme precipitation indices reached their highest values during La Niña events coinciding with a negative Dipole phase. However, several indices also reached their maximum values during Pacific SST neutrality years. In contrast, minimum values were more frequent during climate neutrality periods, covering a large part of the regions. The pattern of maximum and minimum values of extreme indices generally followed the trend of correlations with SST anomalies.

The correlations between temperature extremes and SST anomalies in the Pacific and Atlantic Oceans were also significant, with correlation strengths ranging from weak ($\pm$0.20 to $\pm$0.39) to moderate ($\pm$0.40 to $\pm$0.69) and strong ($\pm$0.70 to $\pm$0.89). In the Pacific (Niño 3.4 region), no clear spatial pattern emerged for temperature extremes (Figure 10). The hottest day (TXx) exhibited strong positive correlations in the northeast (NES), while a negative trend was observed in the southeast (SES) (Figure 10a). The coldest day (TXn) and coldest night (TNn) also showed spatial patterns similar to those of SST anomalies in the Niño 3.4 region, with higher positive correlations in SES and SAM, and considerable spatial variability in these regions (Figures 10c and 11d).

In the Northern Atlantic (TNA), the correlations between temperature extremes and SST anomalies displayed significant spatial variability, extending from the north to the south of SA (Figure 11). The hottest day (TXx) showed moderate positive correlations across much of the NSA, SAM, and NES sectors (Figure 11a). Similarly, the diurnal temperature range (DTR) displayed strong positive correlations in NES and SAM, with moderate correlations in other parts of SA (Figure 11e). Heatwave duration (WSDI) was strongly positively correlated with TNA, particularly over the monsoon region (SAM), with more moderate correlations observed in the NES and NSA regions (Figure 11f).

Extreme hot and cold days (TX90p and TX10p) followed similar spatial patterns, though with inverse magnitudes. Hot days (TX90p) were strongly positively correlated with SST anomalies in the Northern Atlantic (TNA) across NES, SAM, and NSA, while cold days (TX10p) showed negative correlations in these regions (Figure 11h,j). Warm and cold nights (TN90p and TN10p) also correlated with TNA, showing similar spatial distributions but with opposite signs. Warm nights (TN90p) were positively correlated in SAM, NSA, and NWS, while cold nights (TN10p) showed strong negative correlations in NES and NSA (Figure 11i,k).

In summary, hot extremes, such as TX90p and TN90p, reached their highest values in the northern regions of South America (NSW, NSA, NES) during strong El Niño events, regardless of the Atlantic Dipole phase (Figure 12). Cold extremes were more pronounced during La Niña events combined with the negative phase of the Dipole, particularly in NSA and NWS. However, many hot and cold extremes also reached their maximum values during neutral climate periods, spanning both the north and south of South America.

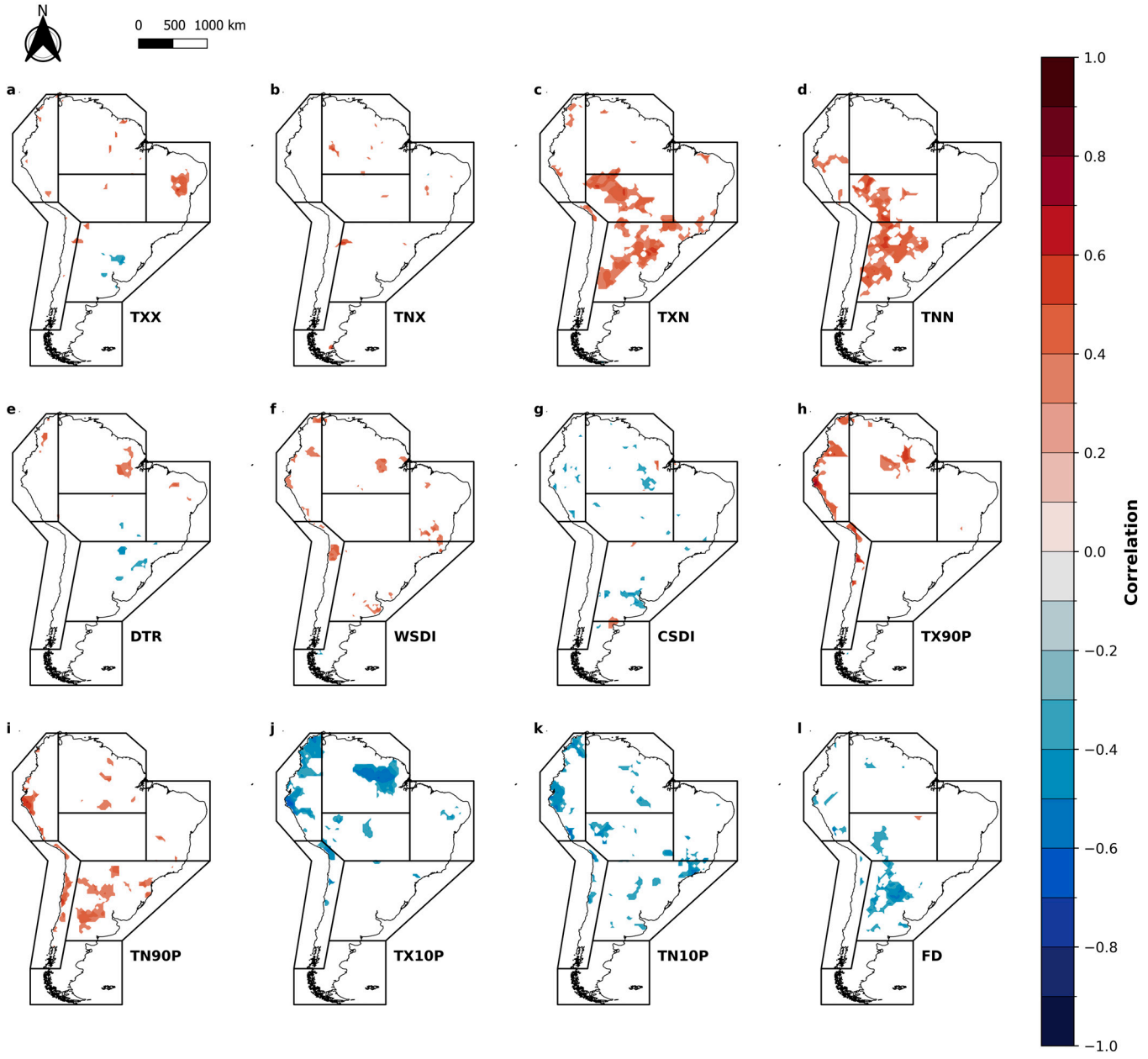

Figure 10. Pearson correlation between sea surface temperature (SST) anomalies in the Pacific Ocean over the Nino 3.4 region and extreme climatic temperature indices: warmest day (TXx) (**a**); warmest night (TNx) (**b**); coldest day (TXn) (**c**); coldest night (TNn) (**d**); diurnal temperature Range (DTR) (**e**); warm spell duration (WSDI) (**f**); cold spell duration (CSDI) (**g**); warm days (TX90p) (**h**); warm nights (TN90p) (**i**); cool days (TX10p) (**j**); cool nights (TN10p) (**k**); and frost days (FD) (**l**) over the climate reference regions of the Sixth Assessment Report of the Intergovernmental Panel on Climate Change (IPCC—AR6) on South America from 1979 to 2020. Only values with statistical significance at the 5% level are presented in the maps.

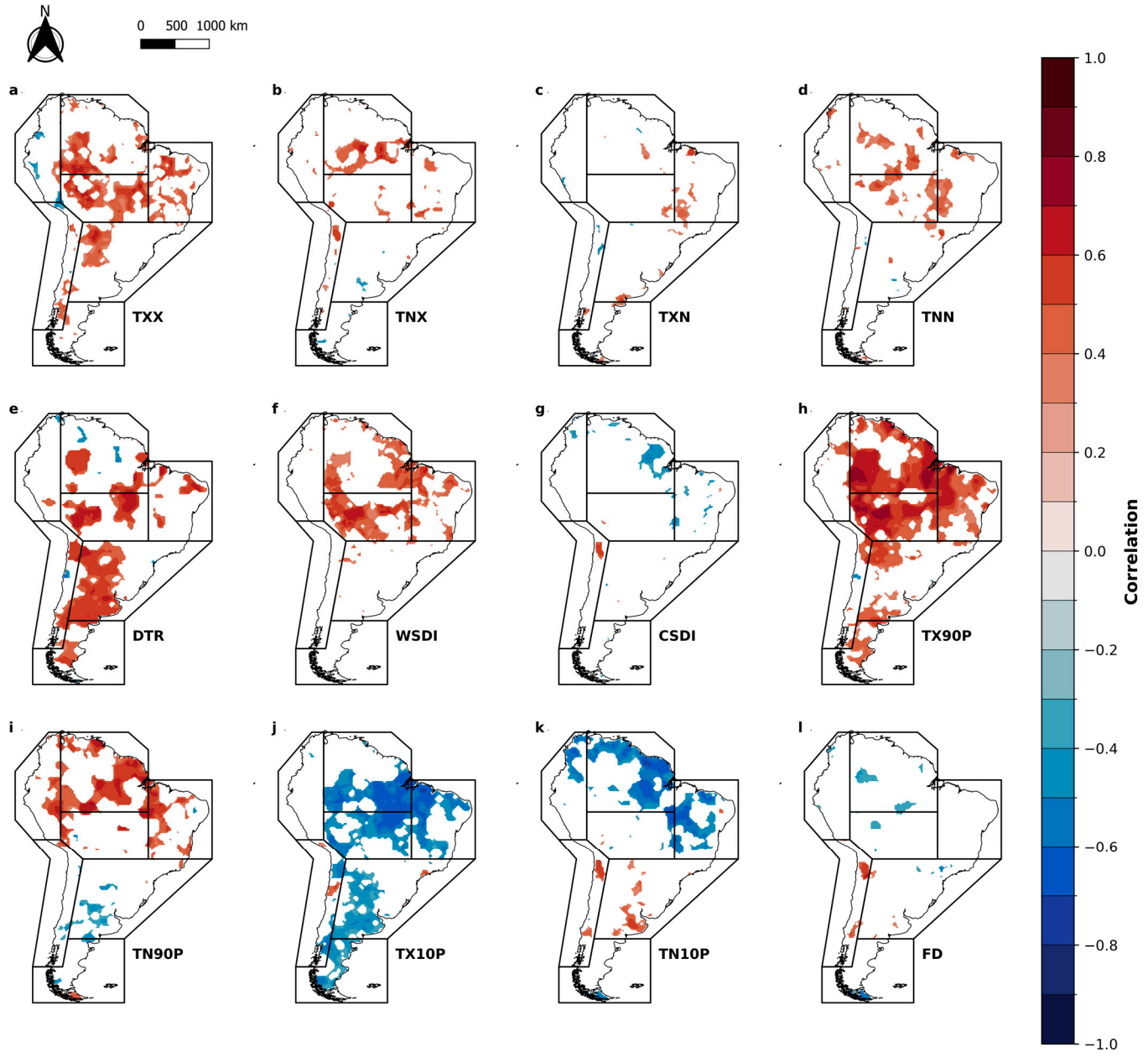

Figure 11. Pearson correlation coefficients between sea surface temperature (SST) anomalies in the Northern Atlantic Ocean (TNA) sector and extreme climatic temperature indices: warmest day (TXx) (**a**); warmest night (TNx) (**b**); coldest day (TXn) (**c**); coldest night (TNn) (**d**); diurnal temperature Range (DTR) (**e**); warm spell duration (WSDI) (**f**); cold spell duration (CSDI) (**g**); warm days (TX90p) (**h**); warm nights (TN90p) (**i**); cool days (TX10p) (**j**); cool nights (TN10p) (**k**); and frost days (FD) (**l**) over the climate reference regions of the Sixth Assessment Report of the Intergovernmental Panel on Climate Change (IPCC—AR6) on South America from 1979 to 2020. Only values with statistical significance at the 5% level are presented in the maps.

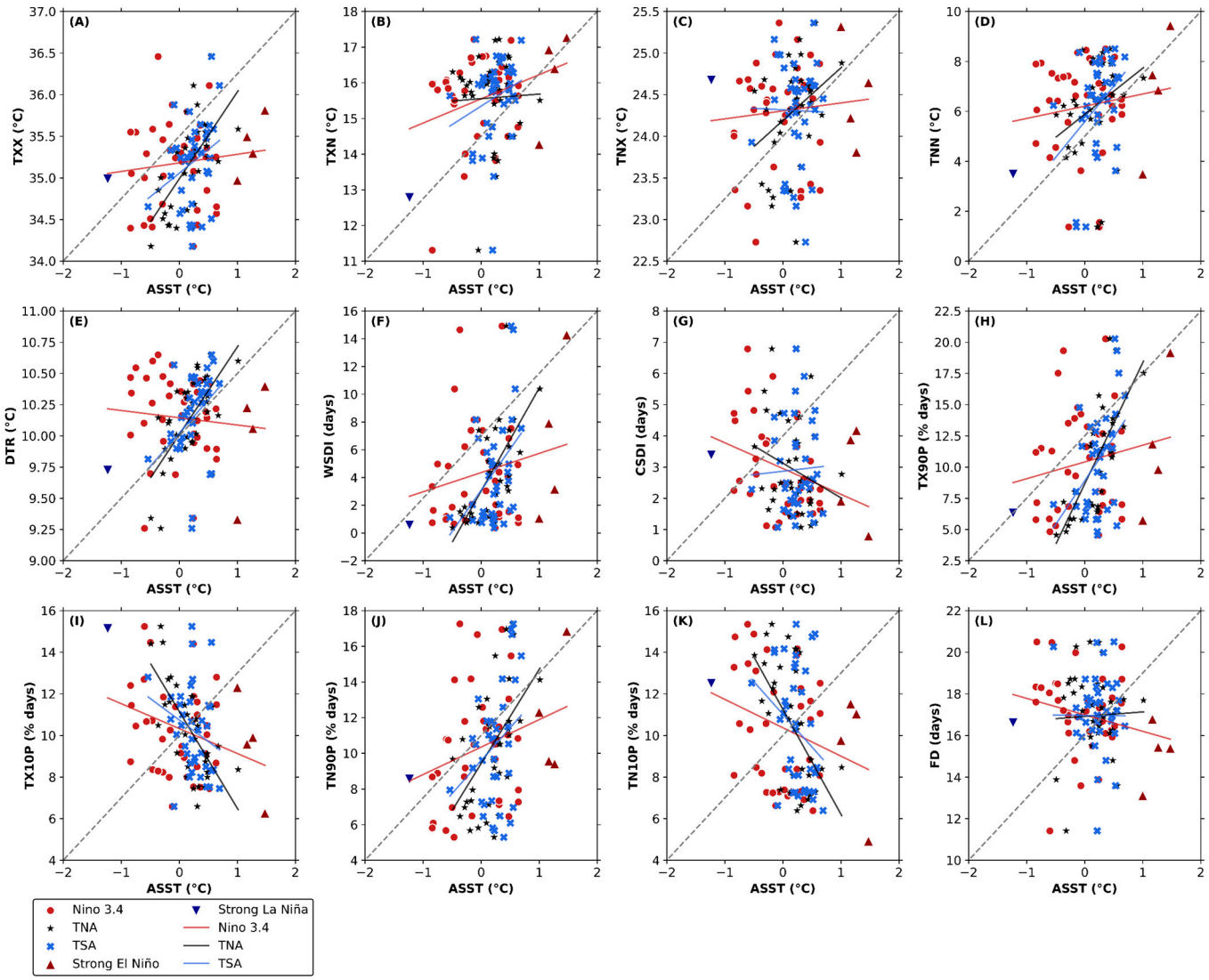

Figure 12. Relationship between sea surface temperature (SST) anomalies in the Pacific Ocean (Niño 3.4), Northern and Southern Atlantic Ocean sectors (TNA) (TSA), and extreme climate temperature indices: warmest day (TXx) (**A**); warmest night (TNx) (**B**); coldest day (TXn) (**C**); coldest night (TNn) (**D**); diurnal temperature Range (DTR) (**E**); warm spell duration (WSDI) (**F**); cold spell duration (CSDI) (**G**); warm days (TX90p) (**H**); warm nights (TN90p) (**I**); cool days (TX10p) (**J**); cool nights (TN10p) (**K**); and frost days (FD) (**L**) over South America from 1979 to 2020.

4. Discussion

4.1. Precipitation and Temperature Extremes Trends

South America has experienced significant shifts in its precipitation patterns, with some regions facing prolonged droughts while others endure more intense rainfall and floods [9]. These changes are influenced by both natural climate variability and human activities. Overall, there has been a decline in total annual precipitation (PRCPTOT) and a reduction in the number of days with heavy rainfall (R10mm, R20mm, and R30mm) across many areas of the continent. However, some regions, particularly in southeastern South America (SES) and parts of the Amazon (NSA and NWS), have seen an increase in extreme precipitation events. Additionally, there is a widespread increase in daily precipitation intensity (SDII), suggesting a shift towards fewer but more intense rainfall events (Figure 3). This variability in precipitation extremes is consistent with the findings from the IPCC AR6 [31].

The observed increase in daily precipitation intensity in regions such as the northwest (NWS), northeast (NES), and southeast (SES) of South America indicates a growing risk of extreme rainfall events, including those with rainfall amounts exceeding the 95th and 99th percentiles (R95p, R99p). These changes, coupled with the sharp decline in consecutive wet days (CWD) and the rise in consecutive dry days (CDD), signal a regional trend toward more pronounced dry spells and shorter, but more intense, periods of rainfall. This pattern heightens the risk of floods and landslides in some areas while increasing drought-related challenges in others.

Regarding temperature extremes, data reveal a clear and widespread warming trend across South America. There has been a consistent increase in the frequency and duration of heat extremes, such as warm days (TX90p) and warm nights (TN90p), alongside a significant reduction in cold events (TX10p, TN10p). The rise in both maximum and minimum temperatures has expanded the diurnal temperature range (DTR), particularly in the southern regions (SES, SSA) and parts of the northeast (NES), where the trend in maximum temperatures is more pronounced. Conversely, in the northern and central regions, the increase in minimum temperatures has been greater, highlighting regional differences in warming patterns (Figure 4). The rise in heat waves, as indicated by the warm spell duration index (WSDI), is particularly notable in the monsoon region (SAM), northeast (NES), and southeast (SES), where heat waves are becoming more frequent and prolonged. Cold spell duration (CSDI), on the other hand, showed little spatial variability, indicating that cold extremes are becoming increasingly rare across the continent.

Land use changes, particularly deforestation in the Amazon and other biomes, may be contributing to these shifts in precipitation and temperature extremes. These changes alter regional climate patterns by affecting the water and energy balance, influencing rainfall distribution, and intensifying temperature extremes [32]. The loss of forest cover reduces moisture recycling and modifies atmospheric circulation patterns, which can exacerbate drought conditions in the Amazon and increase the frequency of extreme heat events [33]. This highlights the need for integrated land management strategies to mitigate the compounding effects of land use change and climate variability on extreme weather events [34,35].

Changes in extreme precipitation patterns are closely linked to variations in global mean surface temperature. The concentration of atmospheric water vapor, which supplies the water for precipitation, increases in proportion to the saturation concentrations at a rate of about 6–7% per degree rise in temperature according to the thermodynamic Clausius–Clapeyron relationship [36,37]. However, these changes in precipitation extremes are also influenced by regional factors such as land use changes, vegetation cover, aerosol emissions, and greenhouse gases. These factors can produce non-local or regionally variable effects, contributing to uncertainties when comparing changes driven by regional processes versus those driven by global thermodynamic forces [38].

Deforestation in the Amazon Basin over recent decades has had significant implications for regional atmospheric circulation and moisture transport [13]. During the boreal summer, a weakening of the northward moisture flux has been observed, while in the austral summer, this flux strengthens toward the south. These changes affect water vapor advection, reducing humidity and moisture recycling in regions such as the western Amazon and the Amazon-Andean transition area (Peru, Bolivia, and Ecuador) [39]. The reduction in moisture recycling, combined with the intensification of upward air motion caused by deforestation, can redistribute and decrease total rainfall in the region. This contributes to more frequent and severe droughts in the south-central Amazon [40].

Shifts in precipitation and temperature extremes have significant impacts on ecological and human systems. If unaddressed, heavy rainfall can lead to floods and landslides, which are already occurring in some regions of South America. Longer droughts can lead to aridification, causing hydrological, agricultural, and ecological droughts, and increasing the risk of wildfires. Extreme heat also poses health risks, such as increased mortality,

disease outbreaks, and higher energy demand, all of which have implications for urban planning and public health systems [35].

4.2. Precipitation and Temperature Extremes and SST Anomalies

Accurate predictions of climate impacts—such as heat waves, frosts, floods, and droughts—are critical for assessing risks to human society and ecosystems. These predictions help improve our understanding of climate impacts and are influenced by several factors, including teleconnections, which refer to relationships between sea surface temperature (SST) anomalies in different regions of the world.

SST anomalies in the Pacific and Atlantic Oceans have both positively and negatively influenced precipitation extremes (R10mm, R20mm, PRCPTOT, SDII, CWD, and CDD) and temperature extremes (TXx, TNn, TX90p, TX10p, TN90p, TN10p, WSDI, and DTR) across large parts of South America. The most pronounced effects of SST anomalies on precipitation extremes were observed in the northern and southern regions of South America, while the central region showed no significant relationship. This lack of correlation in the central region may result from an indirect influence, as ENSO events alter atmospheric systems that affect precipitation patterns.

El Niño events significantly impact atmospheric circulation at multiple levels, leading to either the weakening or strengthening of weather systems, which in turn affects regional and local climate conditions [41]. In the upper atmosphere (200 hPa), El Niño weakens the Bolivian High (BH), a key weather system in the region, during the December-January-February (DJF) period (Figure 14a,b). The BH forms due to intense surface heating over the Bolivian Altiplano, resulting in the formation of convective clouds that generate heavy rainfall [42]. However, during El Niño, this system weakens, which reduces rainfall over the Amazon Basin [43]. When the BH is properly configured, it plays a crucial role in transporting moisture and sustaining precipitation in the Amazon [44].

Additionally, during intense El Niño events, the jet stream over southern South America intensifies at upper levels (200 hPa), which can block the passage of weather systems like cold fronts over Central Brazil and the southern Amazon. This often leads to drought conditions and more frequent extreme heat events in these regions [45]. Furthermore, the trough along the northeastern coast of South America shifts deeper over the South Atlantic during El Niño (Figure 13a,b). This shift is associated with high-pressure systems at lower levels that inhibit convective cloud formation, contributing to droughts in northeast South America (NES) [46].

At mid-level (500 hPa), the semi-permanent South Atlantic High (SASH) usually remains well-defined (Figure 13c). However, during El Niño and when SSTs are warmer in the South Atlantic, this system weakens, allowing subtropical jets near southern Brazil to intensify (Figure 13d). This atmospheric change favors extreme rainfall in southern Brazil, where SASH typically acts as a barrier to precipitation [47]. At surface levels (850 hPa), SASH maintains its climatological position between 20 °S and 40 °S but shows a slight increase in activity during El Niño, which can enhance moisture transport and increase rainfall in southern Brazil (Figure 13f).

In contrast, La Niña episodes exhibit opposite climate patterns [48]. During La Niña, the Bolivian High intensifies and shifts westward toward the Pacific coast (Figure 13c), encouraging the formation of convective clouds and promoting heavy precipitation [49]. At upper levels, subtropical jets over southern Brazil weaken, allowing cold fronts to move into the region more easily, leading to temperature extremes [50]. At mid-levels, the semi-permanent South Atlantic High (SASH) moves inland, increasing the likelihood of drought in southeastern South America (Figure 13f). Additionally, La Niña tends to reduce wind intensity along the northern coast of eastern Amazonia, potentially limiting the inflow of moisture from the Atlantic Ocean into the interior, although this does not necessarily imply drier conditions (Figure 13i).

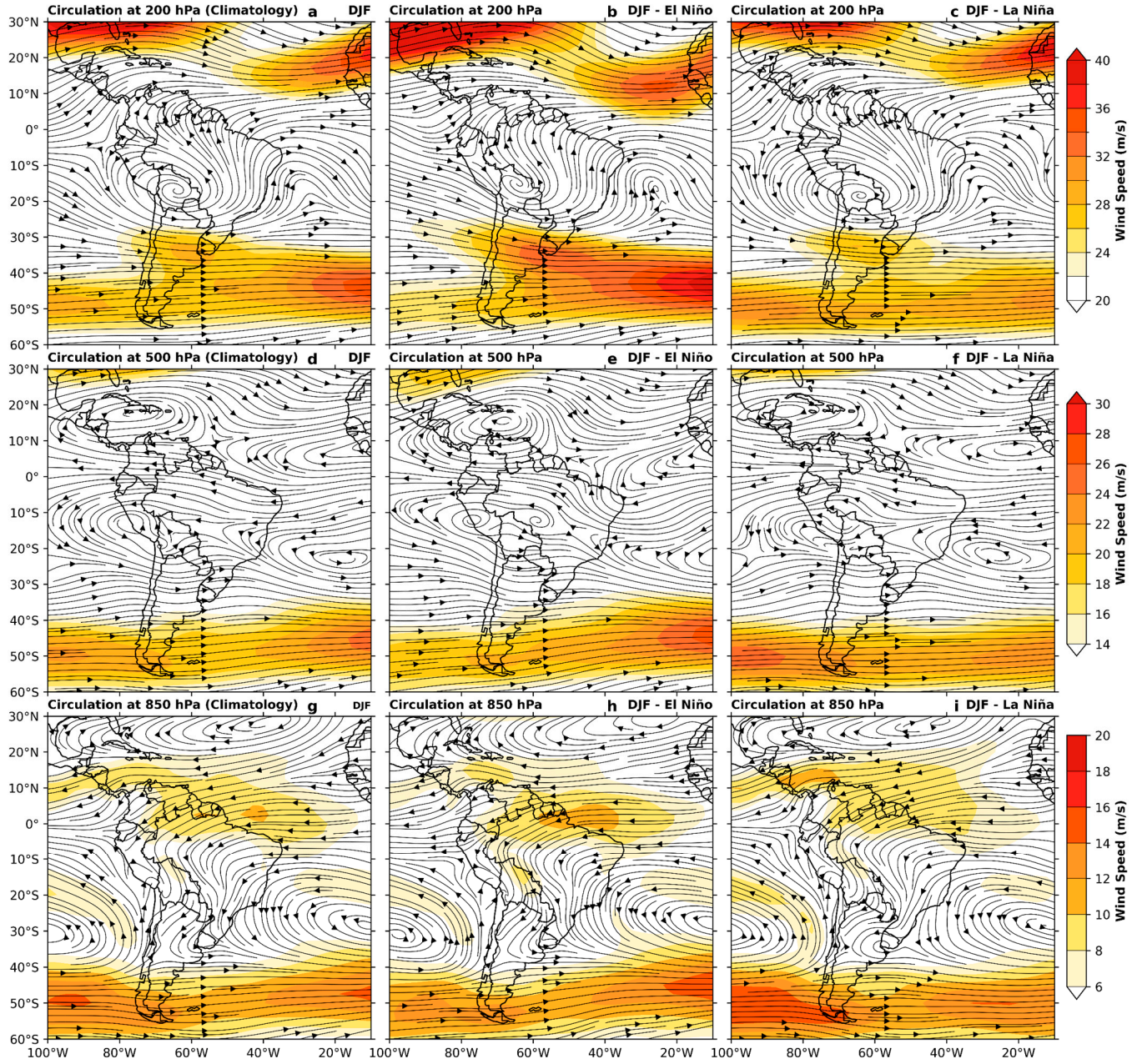

Figure 13. Atmospheric circulation climatology (**a**,**d**,**g**) and observed atmospheric circulation under El Niño (**b**,**e**,**h**) and La Niña (**c**,**f**,**i**) conditions at pressure levels of 200 hPa, 500 hPa, and 850 hPa, respectively, over South America. The shaded region represents wind speed in m s^{-1}. The climatology period is from 1981 to 2010, while the observed data refers to the mean composites of the intense El Niño events in 1982–1983, 1997–1998, and 2015–2016, and La Niña in 1988–1989, 1999–2000, and 2010–2011 in the December–January–February (DJF) quarter.

During La Niña in the June-July-August (JJA) period, an anomalous wind divergence pattern appears at upper levels (200 hPa) over the northern Amazon and northeastern South America (Figure 14a,c). This pattern strengthens surface wind convergence, promoting the formation of convective clouds and increasing rainfall [50]. At mid-levels (500 hPa), the semi-permanent South Atlantic High (SASH) is positioned over the continent during both El Niño and La Niña events (Figure 15e,f). During JJA, SASH prevents polar cold air masses from reaching northern South America, maintaining drier and sunnier conditions in the subtropical region [51]. At surface levels (850 hPa), during La Niña, the SASH center moves closer to the coast, with intensified circulation extending from the southeast

to the southern Amazon (Figure 14i). A strong trough over central-southern Brazil also reinforces subsidence, leading to negative precipitation anomalies and higher temperatures in the region.

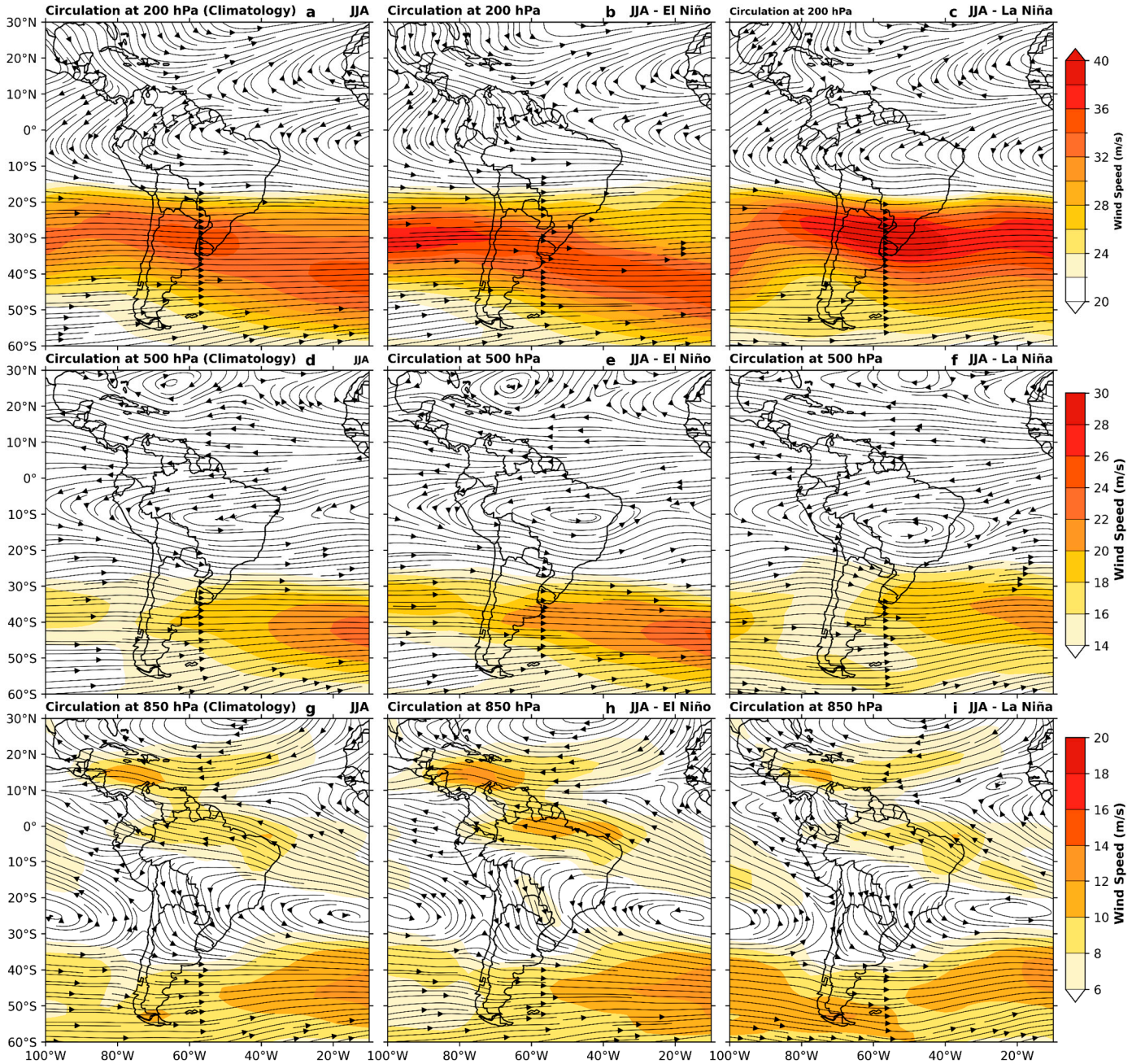

Figure 14. Atmospheric circulation climatology (**a**,**d**,**g**) and observed atmospheric circulation under El Niño (**b**,**e**,**h**) and La Niña (**c**,**f**,**i**) conditions at pressure levels of 200 hPa, 500 hPa, and 850 hPa, respectively, over South America. The shaded region represents wind speed in m s^{-1}. The climatology period is from 1981 to 2010, while the observed data refers to the mean composites of the intense El Niño events in 1982–1983, 1997–1998, and 2015–2016 and La Niña in 1988–1989, 1999–2000, and 2010–2011 in the June–July–August (JJA) quarter.

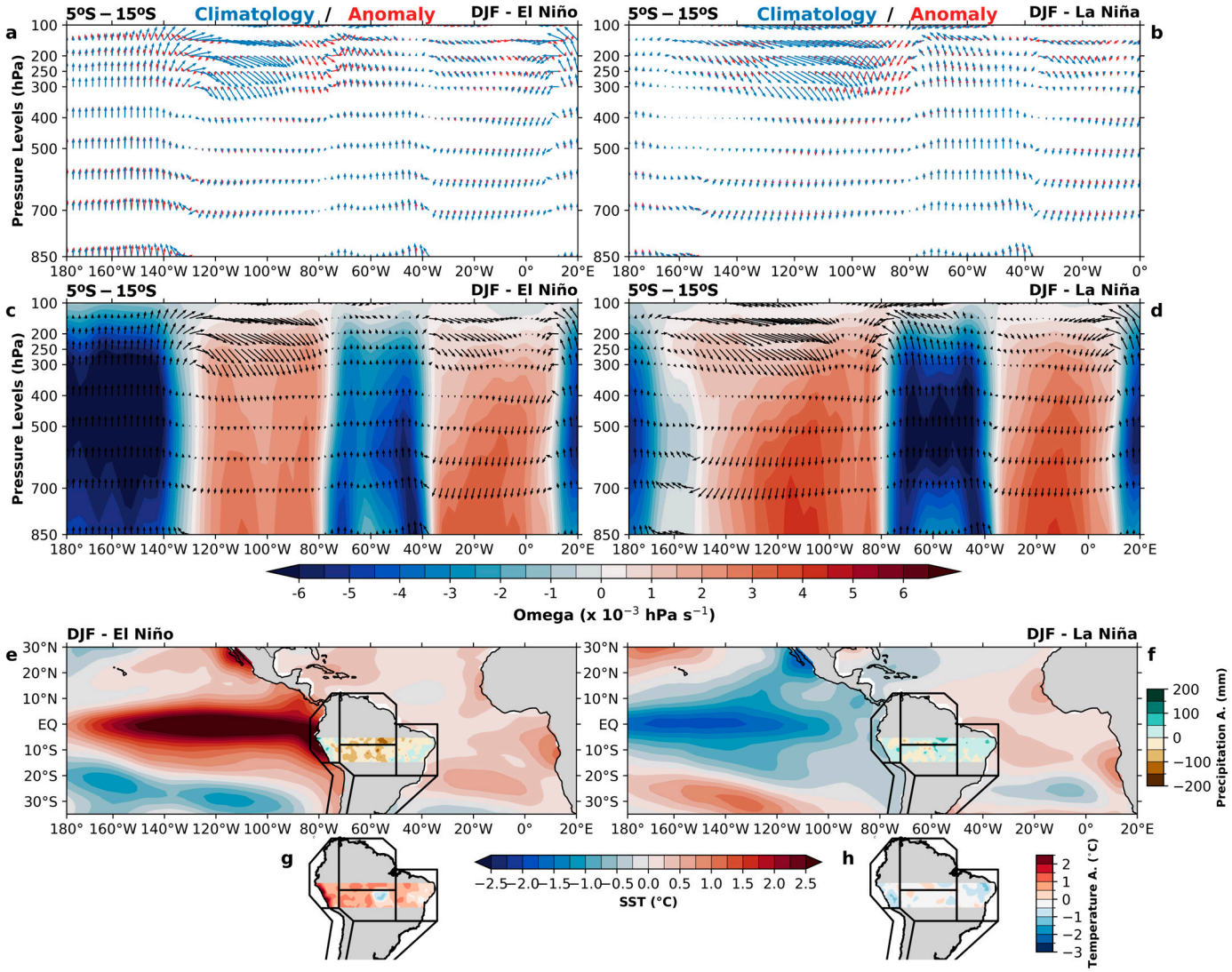

Figure 15. Climatology (blue vectors) and anomaly (red vectors) of vertical wind velocity between 5 °S and 15°S during El Niño (**a**) and La Niña (**b**) events in the December-January-February (DJF) quarter. (**c**,**d**) Vertical wind speed (filled contours) and wind direction (arrows) between 5 °S and 15 °S during El Niño (**c**) and La Niña (**d**) events in the DJF quarter. (**e**,**f**) Sea surface temperature (SST) anomalies and precipitation anomalies over the continent between 5 °S and 15 °S during El Niño (**e**) and La Niña (**f**) events in the DJF quarter. (**g**,**h**) Air temperature anomalies over the continent between 5 °S and 15 °S during El Niño (**g**) and La Niña (**h**) events in the DJF quarter. Data correspond to the composite averages of El Niño (1982–1983, 1997–1998, and 2015–2016) and La Niña (1988–1989, 1999–2000, and 2010–2011) events in the DJF quarter.

El Niño weakens upward vertical motion in the region between 5°S and 15°S, enhancing subsidence and causing negative precipitation anomalies and higher temperatures (Figure 15a,c,e,g). During La Niña, vertical motion intensifies, favoring deep convection and leading to above-average rainfall (Figure 15b,d,f,h). However, La Niña may also result in negative precipitation anomalies in central and western regions, linked to stronger subsidence at higher levels, which limits deep convection and reduces rainfall.

A clear relationship emerges between vertical motion patterns (omega) and precipitation and temperature anomalies during ENSO phases in northern and southern South America. El Niño is generally associated with negative precipitation anomalies in the north and positive anomalies in the south, while La Niña exhibits the opposite pattern [52]. ENSO profoundly influences South America's climate by modulating a complex array of

meteorological processes, including coastal convection, Walker circulation variations, and atmospheric circulation anomalies associated with the Rossby wave train [16].

During the JJA season, the Walker cell showed a pattern of descending vertical motion in the region between 5 °S and 15 °S, even during El Niño events (Figure 16a,c). This downward motion likely suppressed deep convection and cloud formation, leading to negative precipitation anomalies, although these anomalies were relatively small in magnitude (Figure 16e). In contrast, positive air temperature anomalies were observed (Figure 16g). During La Niña, a similar descending vertical motion pattern was observed in the same region (Figure 16b,d), influencing both precipitation and air temperature anomalies. However, it is important to note that the magnitudes of these anomalies during La Niña were closer to normal (Figure 16f,h).

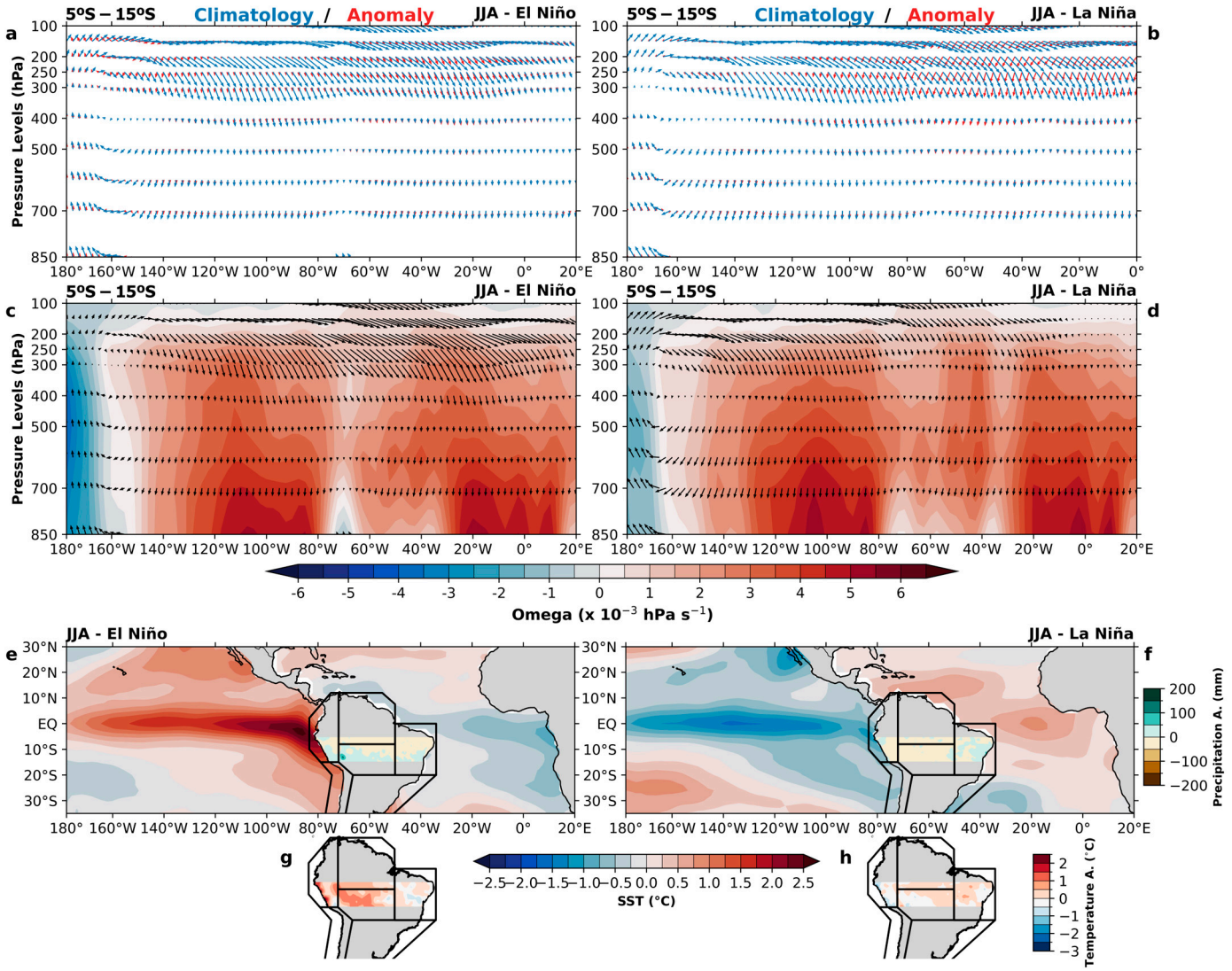

Figure 16. Climatology (blue vectors) and anomaly (red vectors) of vertical wind velocity between 5 °S and 15 °S during El Niño (**a**) and La Niña (**b**) events in the June-July-August (JJA) quarter. (**c**,**d**) Vertical wind speed (filled contours) and wind direction (vectors) between 5 °S and 15 °S during El Niño (**c**) and La Niña (**d**) events in the JJA quarter. (**e**,**f**) Sea surface temperature (SST) anomalies and precipitation anomalies over the continent between 5 °S and 15 °S during El Niño (**e**) and La Niña (**f**) events in the JJA quarter. (**g**,**h**) Air temperature anomalies over the continent between 5 °S and 15 °S during El Niño (**g**) and La Niña (**h**) events in the JJA quarter. Data correspond to the composite averages of El Niño (1982–1983, 1997–1998, and 2015–2016) and La Niña (1988–1989, 1999–2000, and 2010–2011) events in the JJA quarter.

4.3. The Tropical Atlantic Dipole Pattern and Its Climate Implications for South America

The Tropical Atlantic Dipole (TAD), characterized by a meridional gradient in sea surface temperature (SST) between the Northern and Southern Atlantic, has significant climate implications for South America [53]. During the positive phase of the TAD (TNA(+) and TSA(−)), atmospheric circulation over the North Atlantic shows a thermally direct pattern, with rising air over regions of warmer SST in the north and descending air in the south. This circulation contributes to drought intensification in the northern part of Northeast Brazil and the Amazon by reducing evaporation and moisture convergence. In the negative phase of the TAD (TNA(−) and TSA(+)), the circulation reverses, affecting the Intertropical Convergence Zone (ITCZ) and altering the spatial and temporal distribution of precipitation in areas such as the eastern Amazon and Northeast Brazil. The anomalous surface wind and pressure patterns also influence the north-south migration of the ITCZ [54].

The South Atlantic Subtropical Dipole (SAD) is the dominant ocean-atmosphere variability pattern in the South Atlantic [55]. This dipole, oriented northeast-southwest, has centers of action over the tropical and extratropical South Atlantic (SSTA and SESA, respectively) [56]. The SAD is closely linked to the variability of the South Atlantic Subtropical High (SASH), which modulates atmospheric circulation and the oceanic mixed layer [57]. This variability has significant impacts on regional climate, especially during negative phases, when changes in precipitation and temperature patterns are more pronounced over South America [58].

During positive SAD events, cold SST anomalies occur south of 35°S during the austral summer, while the rest of the basin experiences warming. SST and wind anomalies shift northward in the following season, with cyclonic wind stress in the northern part of the SAD leading to increased warming [47]. Negative (positive) SAD events are characterized by positive (negative) sea level pressure (SLP) anomalies across the South Atlantic and negative (positive) SST anomalies over the TSA and along the African coast [59].

El Niño impacts the tropical Atlantic by warming the tropical North Atlantic, typically from late boreal winter to early spring [60]. This warming is driven by the tropospheric temperature mechanism and teleconnections via the Pacific/North American (PNA) pattern [61]. During El Niño, the Atlantic Walker circulation strengthens in response to equatorial Pacific warming generating strong easterly winds over the equatorial Atlantic, which result in cold SST anomalies in the tropical South Atlantic. Concurrently, the PNA pattern induces lower-than-average atmospheric pressures over the southeastern U.S., extending into the North Atlantic, weakening the North Atlantic Subtropical High and reducing trade winds, which lowers evaporative cooling and warms the tropical North Atlantic through wind-evaporation-SST feedback [62]. This generates strong low-level easterly winds over the equatorial Atlantic, resulting in cold SST anomalies in the equatorial and part of the tropical South Atlantic. At the same time, a PNA pattern is induced, with below-average atmospheric pressures over the southeastern United States extending towards the North Atlantic. This warming creates an inter-hemispheric SST gradient known as the Atlantic Meridional Mode (AMM), which shifts the ITCZ north or south, affecting precipitation patterns in northeastern Brazil and West Africa [63]. However, not all ENSO events result in AMM anomalies due to the intrinsic variability of the Atlantic, and ENSO diversity also leads to varied impacts on the tropical Atlantic [64].

The interaction between El Niño and Atlantic Dipole events, whether positive or negative, can create rainfall deficits in Northeast Brazil and the Amazon, although positive precipitation anomalies may occur in parts of the Northeast [65]. Conversely, the South and Southeast regions of South America may experience increased rainfall. During La Niña, when combined with a positive dipole (TNA(+) and TSA(−)), wetter conditions can prevail in central-southern Brazil, while the Northeast and Amazon may become drier [66]. However, if La Niña coincides with a negative dipole (TNA < TSA), the Northeast and Amazon may see more rainfall, while the southeast experiences drought.

During La Niña, South American precipitation is strongly linked to variability in the South Tropical Atlantic (TSA), while El Niño events amplify the effects of positive TSA. This relationship stems from shifts in the ITCZ, which affects both the Hadley and Walker cells, intensifying rainfall anomalies in Northeast Brazil and the Amazon. Studies also show that ENSO and TSA jointly influence water dynamics in the Amazon Basin, particularly during the peak rainfall period (February to May). The TSA has a greater influence on moisture contributions from the Atlantic to the Amazon, while ENSO variability affects moisture transport from the basin to the subtropics [66]. During El Niño and positive Dipole years, moisture largely comes from the TSA, while during La Niña and negative Dipole years, the North Atlantic becomes the main moisture source [64].

5. Conclusions

South America is undergoing substantial changes in climate extremes, with notable shifts in both precipitation and temperature patterns. A general decline in annual precipitation has been observed across much of the continent; however, certain regions—particularly in the northeast and southeast—are experiencing more frequent and intense precipitation events. This shift indicates a redistribution of rainfall patterns, with a tendency toward fewer but more intense precipitation events in specific areas.

Temperature extremes reveal a clear warming trend across South America, marked by an increase in both the frequency and duration of heat events, such as heatwaves and warm nights. This intensification of temperature extremes reflects ongoing global warming, with varying impacts across regions. The increased frequency of warm days and nights, coupled with the decline in cold events, highlights the complexity of climate responses across the continent.

The analysis shows that sea surface temperature (SST) anomalies in the Pacific and Atlantic Oceans play a significant role in driving these climate extremes. Precipitation indices, such as intense rainfall days (R10mm) and total wet-day precipitation (PRCPTOT), respond distinctly to the phases of El Niño and La Niña. La Niña events are associated with higher rainfall frequency and intensity in the northern and northeastern regions, while El Niño and SST-neutral phases tend to correlate with extended dry periods.

Temperature extremes, including indices like TX90p (warm days), TN90p (warm nights), and RX5day (maximum 5-day rainfall), are also influenced by ocean temperature variations. Heatwave duration, measured by the warm spell duration index (WSDI), tends to increase in response to positive phases of the Atlantic Dipole and El Niño events, particularly in the northeast, southeast, and South American monsoon regions. These areas are experiencing more frequent and prolonged heatwaves, while cold nights (TN10p) are becoming increasingly rare.

These findings underscore the importance of understanding SST anomalies as mechanisms driving climate variability in South America. This understanding is essential for informing effective adaptation and mitigation strategies to address the impacts of climate change. Enhanced insight into these interactions will allow for more accurate predictions of climate extremes, aiding policymakers and resource managers in their efforts to protect both human and environmental systems across South America.

Author Contributions: Conceptualization, L.O.F.d.S., N.G.M. and M.S.B.; methodology, L.O.F.d.S., N.G.M., C.A.S.Q. and M.S.B.; software, L.O.F.d.S.; validation, L.O.F.d.S., N.G.M., C.A.S.Q. and M.S.B.; formal analysis, L.O.F.d.S.; investigation, L.O.F.d.S., N.G.M., C.A.S.Q. and M.S.B.; resources, N.G.M. and M.S.B.; data curation, L.O.F.d.S.; writing—original draft preparation, L.O.F.d.S.; writing—review and editing, L.O.F.d.S., N.G.M., C.A.S.Q. and M.S.B.; visualization, L.O.F.d.S., N.G.M., C.A.S.Q. and M.S.B.; supervision, N.G.M. and M.S.B.; project administration, N.G.M. and M.S.B.; funding acquisition, N.G.M. and M.S.B. All authors have read and agreed to the published version of the manuscript.

Funding: This research was partially funded by Conselho Nacional de Desenvolvimento Científico e Tecnológico (CNPq), code #311541/2021-6 and #311907/2021-0, Universidade Federal de Mato Grosso (UFMT), Programa de Pós-Graduação em Física Ambiental (PPGFA/IF/UFMT) and Instituto Federal de Mato Grosso (IFMT).

Data Availability Statement: All data used in this study are available from the Climate Prediction Center of National Oceanic and Atmospheric Administration (NOAA) (https://psl.noaa.gov/data/gridded/, accessed on 21 September 2024).

Acknowledgments: The authors are thankful to the Research Support Foundation of the Amazonas State—FAPEAM for the support provided through the qualification promotion via Call No. 012/2021–POSGFE, which granted a doctoral scholarship to the first author of this study. The authors also are thankful to the National Oceanic and Atmospheric Administration (NOAA) for providing data and the Expert Team on Climate Change Detection Monitoring and Indices (ETCCDMI) for providing the code.

Conflicts of Interest: The authors declare no conflicts of interest. The funders had no role in the design of the study; in the collection, analyses, or interpretation of data; in the writing of the manuscript; or in the decision to publish the results.

References

1. Khan, M.M.H.; Bryceson, I.; Kolivras, K.N.; Faruque, F.; Rahman, M.M.; Haque, U. Natural Disasters and Land-Use/Land-Cover Change in the Southwest Coastal Areas of Bangladesh. *Reg. Environ. Chang.* **2015**, *15*, 241–250. [CrossRef]
2. Reboita, M.S.; Kuki, C.A.C.; Marrafon, V.H.; de Souza, C.A.; Ferreira, G.W.S.; Teodoro, T.; Lima, J.W.M. South America Climate Change Revealed through Climate Indices Projected by GCMs and Eta-RCM Ensembles. *Clim. Dyn.* **2022**, *58*, 459–485. [CrossRef]
3. Costa, R.L.; Macedo de Mello Baptista, G.; Gomes, H.B.; Daniel dos Santos Silva, F.; Lins da Rocha Júnior, R.; de Araújo Salvador, M.; Herdies, D.L. Analysis of Climate Extremes Indices over Northeast Brazil from 1961 to 2014. *Weather Clim. Extrem.* **2020**, *28*, 100254. [CrossRef]
4. Ray, D.K.; West, P.C.; Clark, M.; Gerber, J.S.; Prishchepov, A.V.; Chatterjee, S. Climate Change Has Likely Already Affected Global Food Production. *PLoS ONE* **2019**, *14*, e0217148. [CrossRef] [PubMed]
5. Daher, B.; Hamie, S.; Pappas, K.; Nahidul Karim, M.; Thomas, T. Toward Resilient Water-Energy-Food Systems under Shocks: Understanding the Impact of Migration, Pandemics, and Natural Disasters. *Sustainability* **2021**, *13*, 9402. [CrossRef]
6. Afjal Hossain, M.; Imran Reza, M.; Rahman, S.; Kayes, I. Climate Change and Its Impacts on the Livelihoods of the Vulnerable People in the Southwestern Coastal Zone in Bangladesh. In *Climate Change and the Sustainable Use of Water Resources*; Leal Filho, W., Ed.; Climate Change Management; Springer: Berlin/Heidelberg, Germany, 2012; pp. 237–259. ISBN 978-3-642-22266-5.
7. dos Santos, C.A.C.; Neale, C.M.U.; Mekonnen, M.M.; Gonçalves, I.Z.; de Oliveira, G.; Ruiz-Alvarez, O.; Safa, B.; Rowe, C.M. Trends of Extreme Air Temperature and Precipitation and Their Impact on Corn and Soybean Yields in Nebraska, USA. *Theor. Appl. Climatol.* **2022**, *147*, 1379–1399. [CrossRef]
8. Gleixner, S.; Demissie, T.; Diro, G.T. Did ERA5 Improve Temperature and Precipitation Reanalysis over East Africa? *Atmosphere* **2020**, *11*, 996. [CrossRef]
9. Morales, M.S.; Cook, E.R.; Barichivich, J.; Christie, D.A.; Villalba, R.; LeQuesne, C.; Srur, A.M.; Ferrero, M.E.; González-Reyes, Á.; Couvreux, F.; et al. Six Hundred Years of South American Tree Rings Reveal an Increase in Severe Hydroclimatic Events since Mid-20th Century. *Proc. Natl. Acad. Sci. USA* **2020**, *117*, 16816–16823. [CrossRef]
10. Anjos, L.J.S.; Toledo, P.M. de Measuring Resilience and Assessing Vulnerability of Terrestrial Ecosystems to Climate Change in South America. *PLoS ONE* **2018**, *13*, e0194654. [CrossRef]
11. de Souza, I.P.; Andreoli, R.V.; Kayano, M.T.; Vargas, F.F.; Cerón, W.L.; Martins, J.A.; Freitas, E.; de Souza, R.A.F. Seasonal Precipitation Variability Modes over South America Associated to El Niño-Southern Oscillation (ENSO) and Non-ENSO Components during the 1951–2016 Period. *Int. J. Climatol.* **2021**, *41*, 4321–4338. [CrossRef]
12. Dunn, R.J.H.; Alexander, L.V.; Donat, M.G.; Zhang, X.; Bador, M.; Herold, N.; Lippmann, T.; Allan, R.; Aguilar, E.; Barry, A.A.; et al. Development of an Updated Global Land In Situ-Based Data Set of Temperature and Precipitation Extremes: HadEX3. *J. Geophys. Res. Atmos.* **2020**, *125*, e2019JD032263. [CrossRef]
13. Ruiz-Vásquez, M.; Arias, P.A.; Martínez, J.A.; Espinoza, J.C. Effects of Amazon Basin Deforestation on Regional Atmospheric Circulation and Water Vapor Transport towards Tropical South America. *Clim. Dyn.* **2020**, *54*, 4169–4189. [CrossRef]
14. Collazo, S.; Barrucand, M.; Rusticucci, M. Evaluation of CMIP6 Models in the Representation of Observed Extreme Temperature Indices Trends in South America. *Clim. Chang.* **2022**, *172*, 21. [CrossRef]
15. Ghaedamini, H.A.; Morid, S.; Nazemosadat, M.J.; Shamsoddini, A.; Moghadam, H.S. Validation of the CHIRPS and CPC-Unified Products for Estimating Extreme Daily Precipitation over Southwestern Iran. *Theor. Appl. Climatol.* **2021**, *146*, 1207–1225. [CrossRef]
16. Cai, W.; McPhaden, M.J.; Grimm, A.M.; Rodrigues, R.R.; Taschetto, A.S.; Garreaud, R.D.; Dewitte, B.; Poveda, G.; Ham, Y.-G.; Santoso, A.; et al. Climate Impacts of the El Niño–Southern Oscillation on South America. *Nat. Rev. Earth Environ.* **2020**, *1*, 215–231. [CrossRef]
17. Trenberth, K.E. ENSO in the Global Climate System. In *El Niño Southern Oscillation in a Changing Climate*; American Geophysical Union (AGU): Hoboken, NJ, USA, 2020; pp. 21–37. ISBN 978-1-119-54816-4.
18. Leyba, I.M.; Solman, S.A.; Saraceno, M.; Martinez, J.A.; Dominguez, F. The South Atlantic Ocean as a Moisture Source Region and Its Relation with Precipitation in South America. *Clim. Dyn.* **2023**, *61*, 1741–1756. [CrossRef]

19. Iturbide, M.; Gutiérrez, J.M.; Alves, L.M.; Bedia, J.; Cerezo-Mota, R.; Cimadevilla, E.; Cofiño, A.S.; Di Luca, A.; Faria, S.H.; Gorodetskaya, I.V.; et al. An Update of IPCC Climate Reference Regions for Subcontinental Analysis of Climate Model Data: Definition and Aggregated Datasets. *Earth Syst. Sci. Data* **2020**, *12*, 2959–2970. [CrossRef]
20. Nashwan, M.S.; Shahid, S.; Chung, E.-S. Development of High-Resolution Daily Gridded Temperature Datasets for the Central North Region of Egypt. *Sci. Data* **2019**, *6*, 138. [CrossRef]
21. Sun, Q.; Miao, C.; Duan, Q.; Ashouri, H.; Sorooshian, S.; Hsu, K.-L. A Review of Global Precipitation Data Sets: Data Sources, Estimation, and Intercomparisons. *Rev. Geophys.* **2018**, *56*, 79–107. [CrossRef]
22. Huang, B.; Thorne, P.W.; Banzon, V.F.; Boyer, T.; Chepurin, G.; Lawrimore, J.H.; Menne, M.J.; Smith, T.M.; Vose, R.S.; Zhang, H.-M. Extended Reconstructed Sea Surface Temperature, Version 5 (ERSSTv5): Upgrades, Validations, and Intercomparisons. *J. Clim.* **2017**, *30*, 8179–8205. [CrossRef]
23. Wong, A.P.S.; Wijffels, S.E.; Riser, S.C.; Pouliquen, S.; Hosoda, S.; Roemmich, D.; Gilson, J.; Johnson, G.C.; Martini, K.; Murphy, D.J.; et al. Argo Data 1999–2019: Two Million Temperature-Salinity Profiles and Subsurface Velocity Observations from a Global Array of Profiling Floats. *Front. Mar. Sci.* **2020**, *7*, 700. [CrossRef]
24. Avila-Diaz, A.; Benezoli, V.; Justino, F.; Torres, R.; Wilson, A. Assessing Current and Future Trends of Climate Extremes across Brazil Based on Reanalyses and Earth System Model Projections. *Clim. Dyn.* **2020**, *55*, 1403–1426. [CrossRef]
25. Mengistu, A.G.; Tesfuhuney, W.A.; Woyessa, Y.E.; van Rensburg, L.D. Analysis of the Spatio-Temporal Variability of Precipitation and Drought Intensity in an Arid Catchment in South Africa. *Climate* **2020**, *8*, 70. [CrossRef]
26. Sun, Q.; Zhang, X.; Zwiers, F.; Westra, S.; Alexander, L.V. A Global, Continental, and Regional Analysis of Changes in Extreme Precipitation. *J. Clim.* **2021**, *34*, 243–258. [CrossRef]
27. Bari, S.H.; Rahman, M.T.U.; Hoque, M.A.; Hussain, M.M. Analysis of Seasonal and Annual Rainfall Trends in the Northern Region of Bangladesh. *Atmos. Res.* **2016**, *176–177*, 148–158. [CrossRef]
28. Dos Santos, C.A.C.; Melo, M.M.M.S.; de Brito, J.I.B. Tendências de Índices de Extremos Climáticos para o Estado do Amazonas e suas Relações com a TSM dos Oceanos Tropicais. *Rev. Bras. Meteorol.* **2016**, *31*, 1–10. [CrossRef]
29. Bretherton, C.S.; Widmann, M.; Dymnikov, V.P.; Wallace, J.M.; Bladé, I. The Effective Number of Spatial Degrees of Freedom of a Time-Varying Field. *J. Clim.* **1999**, *12*, 1990–2009. [CrossRef]
30. Pavlides, A.; Agou, V.D.; Hristopulos, D.T. Non-Parametric Kernel-Based Estimation and Simulation of Precipitation Amount. *J. Hydrol.* **2022**, *612*, 127988. [CrossRef]
31. Castellanos, E.J.; Lemos, M.F. *IPCC Sixth Assessment Report (AR6): Climate Change 2022—Impacts, Adaptation and Vulnerability: Regional Factsheet Central and South America*; Cambridge University Press: Cambridge, UK, 2022.
32. Jin, X.; Jiang, P.; Du, H.; Chen, D.; Li, M. Response of Local Temperature Variation to Land Cover and Land Use Intensity Changes in China over the Last 30 Years. *Clim. Chang.* **2021**, *164*, 34. [CrossRef]
33. Salazar, A.; Baldi, G.; Hirota, M.; Syktus, J.; McAlpine, C. Land Use and Land Cover Change Impacts on the Regional Climate of Non-Amazonian South America: A Review. *Glob. Planet. Chang.* **2015**, *128*, 103–119. [CrossRef]
34. Biudes, M.S.; Geli, H.M.E.; Vourlitis, G.L.; Machado, N.G.; Pavão, V.M.; dos Santos, L.O.F.; Querino, C.A.S. Evapotranspiration Seasonality over Tropical Ecosystems in Mato Grosso, Brazil. *Remote Sens.* **2022**, *14*, 2482. [CrossRef]
35. dos Santos, L.O.F.; Machado, N.G.; Biudes, M.S.; Geli, H.M.E.; Querino, C.A.S.; Ruhoff, A.L.; Ivo, I.O.; Lotufo Neto, N. Trends in Precipitation and Air Temperature Extremes and Their Relationship with Sea Surface Temperature in the Brazilian Midwest. *Atmosphere* **2023**, *14*, 426. [CrossRef]
36. Westra, S.; Alexander, L.V.; Zwiers, F.W. Global Increasing Trends in Annual Maximum Daily Precipitation. *J. Clim.* **2013**, *26*, 3904–3918. [CrossRef]
37. Tabari, H. Climate Change Impact on Flood and Extreme Precipitation Increases with Water Availability. *Sci. Rep.* **2020**, *10*, 13768. [CrossRef]
38. Paik, S.; Min, S.-K.; Zhang, X.; Donat, M.G.; King, A.D.; Sun, Q. Determining the Anthropogenic Greenhouse Gas Contribution to the Observed Intensification of Extreme Precipitation. *Geophys. Res. Lett.* **2020**, *47*, e2019GL086875. [CrossRef]
39. Sierra, J.P.; Junquas, C.; Espinoza, J.C.; Segura, H.; Condom, T.; Andrade, M.; Molina-Carpio, J.; Ticona, L.; Mardoñez, V.; Blacutt, L.; et al. Deforestation Impacts on Amazon-Andes Hydroclimatic Connectivity. *Clim. Dyn.* **2022**, *58*, 2609–2636. [CrossRef]
40. Mu, Y.; Biggs, T.W.; Jones, C. Importance in Shifting Circulation Patterns for Dry Season Moisture Sources in the Brazilian Amazon. *Geophys. Res. Lett.* **2023**, *50*, e2023GL103167. [CrossRef]
41. Tedeschi, R.G.; Cavalcanti, I.F.A.; Grimm, A.M. Influences of Two Types of ENSO on South American Precipitation. *Int. J. Climatol.* **2013**, *33*, 1382–1400. [CrossRef]
42. Meseguer-Ruiz, O.; Ponce-Philimon, P.I.; Baltazar, A.; Guijarro, J.A.; Serrano-Notivoli, R.; Olcina Cantos, J.; Martin-Vide, J.; Sarricolea, P. Synoptic Attributions of Extreme Precipitation in the Atacama Desert (Chile). *Clim. Dyn.* **2020**, *55*, 3431–3444. [CrossRef]
43. Junquas, C.; Li, L.; Vera, C.S.; Le Treut, H.; Takahashi, K. Influence of South America Orography on Summertime Precipitation in Southeastern South America. *Clim. Dyn.* **2016**, *46*, 3941–3963. [CrossRef]
44. Segura, H.; Junquas, C.; Espinoza, J.C.; Vuille, M.; Jauregui, Y.R.; Rabatel, A.; Condom, T.; Lebel, T. New Insights into the Rainfall Variability in the Tropical Andes on Seasonal and Interannual Time Scales. *Clim. Dyn.* **2019**, *53*, 405–426. [CrossRef]

45. Montini, T.L.; Jones, C.; Carvalho, L.M.V. The South American Low-Level Jet: A New Climatology, Variability, and Changes. *J. Geophys. Res. Atmos.* **2019**, *124*, 1200–1218. [CrossRef]
46. de Morais, M.D.C.; Gan, M.A.; Yoshida, M.C. Features of the Upper Tropospheric Cyclonic Vortices of Northeast Brazil in Life Cycle Stages. *Int. J. Climatol.* **2021**, *41*, E39–E58. [CrossRef]
47. Wainer, I.; Prado, L.F.; Khodri, M.; Otto-Bliesner, B. The South Atlantic Sub-Tropical Dipole Mode since the Last Deglaciation and Changes in Rainfall. *Clim. Dyn.* **2021**, *56*, 109–122. [CrossRef]
48. McPhaden, M.J.; Santoso, A.; Cai, W. Introduction to El Niño Southern Oscillation in a Changing Climate. In *El Niño Southern Oscillation in a Changing Climate*; American Geophysical Union (AGU): Hoboken, NJ, USA, 2020; pp. 1–19. ISBN 978-1-119-54816-4.
49. Garreaud, R.D.; Vuille, M.; Compagnucci, R.; Marengo, J. Present-Day South American Climate. *Palaeogeogr. Palaeoclimatol. Palaeoecol.* **2009**, *281*, 180–195. [CrossRef]
50. Marengo, J.A.; Liebmann, B.; Grimm, A.M.; Misra, V.; Silva Dias, P.L.; Cavalcanti, I.F.A.; Carvalho, L.M.V.; Berbery, E.H.; Ambrizzi, T.; Vera, C.S.; et al. Recent Developments on the South American Monsoon System. *Int. J. Climatol.* **2012**, *32*, 1–21. [CrossRef]
51. Lee, S.-K.; Mechoso, C.R.; Wang, C.; Neelin, J.D. Interhemispheric Influence of the Northern Summer Monsoons on Southern Subtropical Anticyclones. *J. Clim.* **2013**, *26*, 10193–10204. [CrossRef]
52. Rehbein, A.; Ambrizzi, T. ENSO Teleconnections Pathways in South America. *Clim. Dyn.* **2023**, *61*, 1277–1292. [CrossRef]
53. Londoño Arteaga, V.; Lima, C.H.R. Analysis of CMIP 5 Simulations of Key Climate Indices Associated with the South America Monsoon System. *Int. J. Climatol.* **2021**, *41*, 404–422. [CrossRef]
54. Martins, G.; von Randow, C.; Sampaio, G.; Dolman, A.J. Precipitation in the Amazon and Its Relationship with Moisture Transport and Tropical Pacific and Atlantic SST from the CMIP5 Simulation. *Hydrol. Earth Syst. Sci. Discuss.* **2015**, *12*, 671–704. [CrossRef]
55. Manta, G.; Bach, E.; Talento, S.; Barreiro, M.; Speich, S.; Ghil, M. The South Atlantic Dipole via Multichannel Singular Spectrum Analysis. *Sci. Rep.* **2024**, *14*, 15534. [CrossRef] [PubMed]
56. Wainer, I.; Prado, L.F.; Khodri, M.; Otto-Bliesner, B. Reconstruction of the South Atlantic Subtropical Dipole Index for the Past 12,000 Years from Surface Temperature Proxy. *Sci. Rep.* **2014**, *4*, 5291. [CrossRef] [PubMed]
57. Zilli, M.T.; Carvalho, L.M.V.; Lintner, B.R. The Poleward Shift of South Atlantic Convergence Zone in Recent Decades. *Clim. Dyn.* **2019**, *52*, 2545–2563. [CrossRef]
58. Reboita, M.S.; Ambrizzi, T.; Silva, B.A.; Pinheiro, R.F.; da Rocha, R.P. The South Atlantic Subtropical Anticyclone: Present and Future Climate. *Front. Earth Sci.* **2019**, *7*. [CrossRef]
59. Flantua, S.G.A.; Hooghiemstra, H.; Vuille, M.; Behling, H.; Carson, J.F.; Gosling, W.D.; Hoyos, I.; Ledru, M.P.; Montoya, E.; Mayle, F.; et al. Climate Variability and Human Impact in South America during the Last 2000 Years: Synthesis and Perspectives from Pollen Records. *Clim. Past* **2016**, *12*, 483–523. [CrossRef]
60. Taschetto, A.S.; Rodrigues, R.R.; Meehl, G.A.; McGregor, S.; England, M.H. How Sensitive Are the Pacific–Tropical North Atlantic Teleconnections to the Position and Intensity of El Niño-Related Warming? *Clim. Dyn.* **2016**, *46*, 1841–1860. [CrossRef]
61. Taschetto, A.S.; Ummenhofer, C.C.; Stuecker, M.F.; Dommenget, D.; Ashok, K.; Rodrigues, R.R.; Yeh, S.-W. ENSO Atmospheric Teleconnections. In *El Niño Southern Oscillation in a Changing Climate*; American Geophysical Union (AGU): Hoboken, NJ, USA, 2020; pp. 309–335. ISBN 978-1-119-54816-4.
62. Sasaki, W.; Doi, T.; Richards, K.J.; Masumoto, Y. The Influence of ENSO on the Equatorial Atlantic Precipitation through the Walker Circulation in a CGCM. *Clim. Dyn.* **2015**, *44*, 191–202. [CrossRef]
63. Vallès-Casanova, I.; Lee, S.-K.; Foltz, G.R.; Pelegrí, J.L. On the Spatiotemporal Diversity of Atlantic Niño and Associated Rainfall Variability Over West Africa and South America. *Geophys. Res. Lett.* **2020**, *47*, e2020GL087108. [CrossRef]
64. Reboita, M.S.; Ambrizzi, T.; Crespo, N.M.; Dutra, L.M.M.; de Ferreira, G.W.S.; Rehbein, A.; Drumond, A.; da Rocha, R.P.; de Souza, C.A. Impacts of Teleconnection Patterns on South America Climate. *Ann. N. Y. Acad. Sci.* **2021**, *1504*, 116–153. [CrossRef]
65. Reboita, M.S.; de Santos, I.A. Influência de alguns padrões de teleconexão na precipitação no norte e nordeste do brasil. *Rev. Bras. Climatol.* **2014**, *15*, 2237–8642. [CrossRef]
66. Drumond, A.; Marengo, J.; Ambrizzi, T.; Nieto, R.; Moreira, L.; Gimeno, L. The Role of the Amazon Basin Moisture in the Atmospheric Branch of the Hydrological Cycle: A Lagrangian Analysis. *Hydrol. Earth Syst. Sci.* **2014**, *18*, 2577–2598. [CrossRef]